Monthly Notices of the ROYAL ASTRONOMICAL SOCIETY

MNRAS **535,** 2189–2209 (2024) https://doi.org/10.1093/mnras/stae2439
Advance Access publication 2024 October 25

Characterizing the features of the low-amplitude peaks in delta Scuti stars with *TESS*

S. Barceló Forteza,[1,2]★ J. Pascual-Granado [2], J. C. Suárez [1], A. García Hernández [1], G. M. Mirouh [1,2] and M. Lares-Martiz [3]

[1]*Departamento de Física Teórica y del Cosmos, Universidad de Granada (UGR), E-18071 Granada, Spain*
[2]*Instituto de Astrofísica de Andalucía (CSIC), Glorieta de la Astronomía s/n, E-18008 Granada, Spain*
[3]*Embry-Riddle Aeronautical University (ERAU), 1 Aerospace Blvd., Daytona Beach, FL 32114, USA*

Accepted 2024 October 18. Received 2024 October 18; in original form 2024 June 28

ABSTRACT

The presence of low-amplitude peaks over the noise in the power spectra of δ Scuti stars is frequently disregarded. These seemingly insignificant peaks, collectively referred to as *grass*, might contain valuable information about the origin of these stars and the reasons behind the occurrence or absence of a plateau. It is crucial to systematically parametrize the grass phenomenon throughout a comprehensive sample that covers the entire δ Scuti star parameter range. Thus, we conduct a quantitative study of long-duration, high-duty-cycle *Transiting Exoplanet Survey Satellite* light curves, leading to improved detection methods for plateaus and a deeper understanding of their nature. This approach minimizes the impact of unresolved peaks caused by mode variations over time. Additionally, we present appropriate analysis techniques to mitigate window effects and identify and eliminate spurious peaks. We demonstrate here that the grass can be effectively parametrized based on peak density. With such parametrization two distinct regimes are found: the *sparse grass regime*, characterized by low peak density and the absence of a plateau in the power spectra, and the *dense grass regime*, characterized by high peak densities and the presence of an observable plateau. Our study is the first rigorous quantification of the emergence of such a plateau in the power spectra of δ Scuti stars. Since the grass might be related with fractality, mode variability, and stellar rotation rate, its parametrization opens a new way to analyse these stars.

Key words: asteroseismology – stars: oscillations (*including pulsations*) – stars: variables: Scuti.

1 INTRODUCTION

The classical stellar pulsators known as δ Scuti stars are A-F intermediate-mass stars (1.5–2.5 $M_\odot$; Breger 2000) with temperatures from 6000 to 9000 K (Uytterhoeven et al. 2011) and frequencies between 50 and 930 μHz. Their main excitation mechanism is known as the κ-mechanism (Chevalier 1971) although other mechanisms may play a significant role (Antoci et al. 2014; Xiong et al. 2016).

Some of the first δ Scuti stars observed by *CoRoT* space telescope (Baglin et al. 2006) present a flat power excess unobservable from the ground, made by a high number of low-amplitude peaks, that sharply decreases at higher frequencies down to noise (Poretti et al. 2009). Fig. 1 shows the power spectrum of a δ Scuti star with plateau. The amplitudes of the peaks are slightly higher than the background noise, but they are still statistically significant.

There are many possible (non-)physical phenomena behind the origin of this power-spectral feature. For example, the plateau may be produced by a cascade bug during the analysis of the data (Balona 2014) or by the possible non-harmonic nature of the observed power spectra (Pascual-Granado, Garrido & Suárez 2015).

This observed rich power spectra of δ Scuti stars may be explained by the presence of very high degree modes ($\ell \lesssim 200$) apart from a few low degree ones with higher amplitudes at lower frequency regimes ($\ell \lesssim 3$; Daszyńska-Daszkiewicz, Dziembowski & Pamyatnykh 2006). This apparently random subset of low-degree modes may be selected by non-linearities due to a collective saturation of the driving mechanism (Nowakowski 2005). In that way, the amplitude decrease of some modes may allow others to be excited.

Split peaks due to mode variations in time are commonly observed since ∼ 45 per cent of the power spectra of *Kepler*δ Scuti stars have one sidelobe (Balona & Dziembowski 2011). This is in agreement with Barceló Forteza et al. (2020) who show that 73 per cent of δ Scuti stars of their ∼2300 star sample present different kinds of split peaks. Each kind may be explained with different mechanisms. These mechanisms can be extrinsic to the modes, such as orbital Doppler effect in multiple systems (Shibahashi & Kurtz 2012), or intrinsic, such as mode coupling (e.g. Moskalik 1985; Buchler, Goupil & Hansen 1997; Barceló Forteza et al. 2015).

Another possible explanation could be a granulation background signal that may develop in cool δ Scuti stars since they could have thin outer convective layers (Kallinger & Matthews 2010; Balona 2011). Another cause may be a misaligned magnetic field from the rotation axis that splits the modes into $(2l + 1)^2$ peaks (Goode & Thompson 1992). However, it may not be common in δ Scuti stars

★ E-mail: sbarcelo@iaa.es

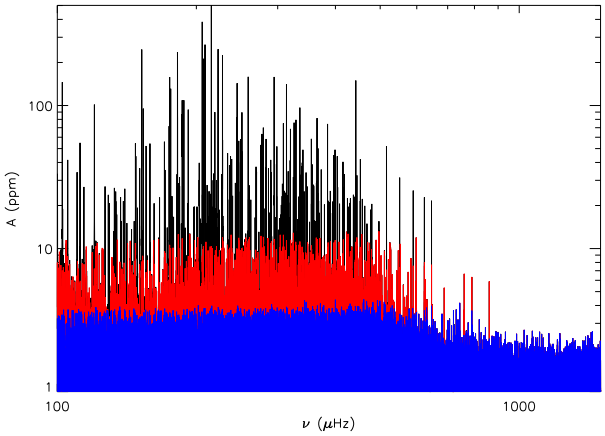

Figure 1. Power spectrum of TIC 198456033, a δ Scuti star with plateau (black). Red points to the contribution of grass peaks. Blue represents the power spectrum below detection limit.

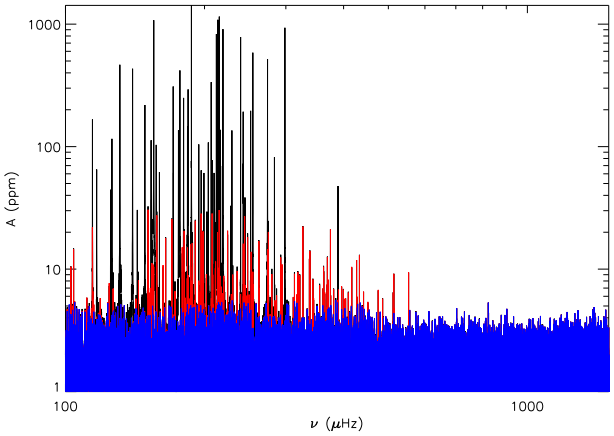

Figure 2. Same as Fig. 1 but for TIC 232604221, a δ Scuti star without plateau.

since only a few detections have been reported (Kurtz et al. 2008; Neiner, Wade & Sikora 2017; Zwintz et al. 2020).

Rotation is one of the most plausible mechanisms. A high rotation rate modifies the shape of the star from a sphere to an oblate spheroid. Owing to the geometry of the star, a less-effective disc-averaging of the flux allows to observe higher degree modes than the spherical case (up to $l = 20$, Kennelly et al. 1998; Poretti et al. 2009). In addition, the oblateness of the star can lead to the emergence of a significant number of chaotic modes (Lignières & Georgeot 2009). Not only moderate to fast rotation is widespread in A-type stars (e.g. Royer, Zorec & Gómez 2007), but also it is related to many of the other phenomena, such as the magnetic fields or the rotational mode coupling (e.g. Soufi, Goupil & Dziembowski 1998).

Each of these physical mechanisms may be of different importance depending on the particular characteristics of each δ Scuti star. In fact, Barceló Forteza et al. (2017, BF2017 hereafter) contends that the two main mechanisms are rotation and mode variation.

To study the low-amplitude peaks of the power spectra, BF2017 defined the so-called grass as the low-amplitude peaks within δ Scuti frequency regime with $S_i \lesssim 0.01$ per cent, where

$$S_i\,(\%) \equiv 100\frac{\mathrm{rms}_i - \mathrm{rms}_{i+1}}{\mathrm{rms}_0}\,, \tag{1}$$

and rms_i is the root mean square of the residual signal before subtracting the i-th peak from the pulsation signature assuming a flux given by

$$F \approx \sum_i A_i \sin\left(2\pi\,\nu_i t + \phi_i\right) + N\,, \tag{2}$$

in which each harmonic signature is characterized by its frequency, amplitude, and phase (ν_i, A_i, and ϕ_i, respectively), and N is the background noise. Then, S_i is the contribution of the peak to the entire light curve. Taking into account its definition, grass peaks may or may not form a plateau. Fig. 1 highlights the dense contribution of the grass to the plateau down to the detection limit. On the contrary, Fig. 2 shows a few scattered grass peaks but no plateau.

This S_i limit is useful to differentiate the grass peaks from those of the envelope with higher amplitudes. The envelope peaks origin is mainly pulsation and they follow several scaling relations such as the low-order large separation – mean density of the star (Suárez et al. 2014; García Hernández et al. 2015, 2017; Bedding et al. 2020), and the temperature, gravity, and frequency at maximum power (e.g. Balona & Dziembowski 2011; Moya et al. 2017; Barceló Forteza, Roca Cortés & García 2018; Bowman & Kurtz 2018; Barceló Forteza et al. 2020; Hasanzadeh, Safari & Ghasemi 2021). BF2017 defined the envelope as the peaks within the δ Scuti pulsation regime with $S_i \gtrsim 0.1$ per cent. The peaks between the upper limit of the grass regime ($S_i \lesssim 0.01$ per cent) and the envelope lower limit may belong to one of these two regimes. They used these different limits to avoid using peaks belonging to the other region that might influence the results. In this work, we will follow these definitions.

BF2017 studied the grass of four δ Scuti stars in order to unveil the characteristics of the plateau. Using the power spectra of the residual light curve after subtracting the envelope, they calculated the mean amplitude of the grass (A_g) and the mean density of plateau peaks ($\bar{n}$). To calculate these values, they take into account the typical frequency regime of δ Scuti pulsations up to the cut-off frequency, ν_c, where the amplitude/density of peaks significantly decay.

Here, we present a quantitative study of the plateau phenomenon that allow its parametrization, improving the understanding of its nature and how it is detected. In Section 2, we introduce our sample of δ Scuti stars in order to cover the most representative cases. We explain how data are analysed including low-duty-cycle light-curve reduction and how its power spectral structure is classified via their signal (S_i, see Section 3). In addition to this formalism, we propose the plateau factor, i.e. the steadiness of the amplitude across the plateau, obtaining two different regimes (see Section 4). Taking into account our results, we discuss the possible mechanisms behind the emergence of the plateau in Section 5. Finally, we present our conclusions in Section 6.

2 DATA FROM SPACE TELESCOPES

The high photometric precision required to study peaks of a few parts-per-million is reached by space telescopes such as *CoRoT* or *Kepler* (Baglin et al. 2006; Borucki et al. 2010). The longer the campaign, the better to avoid unresolved peaks of the power spectrum due to mode variations (BF2017). For example, the 4-yr-long observations of *Kepler* allow us to observe cyclic variations of some δ Scuti star modes with periods up to years (e.g. Barceló Forteza et al. 2015). Nevertheless, *Kepler* long cadence (∼30 min) produces power spectra with lower Nyquist frequency ($\nu_{Ny} \sim 283$ μHz) than the highest frequencies of the typical pulsation regime for δ Scuti stars. These data sets can be used to study high-amplitude peaks via superNyquist asteroseismology (Murphy, Shibahashi & Kurtz 2013), but not for very dense spectra saturated with low-amplitude frequency-blended peaks.

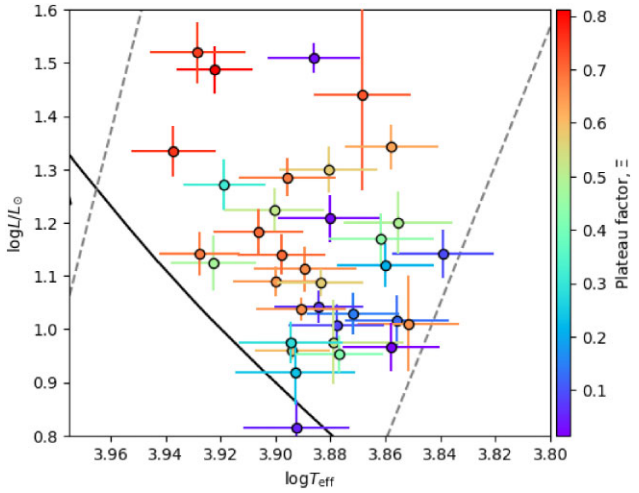

Figure 3. Sample of δ Scuti stars from *TESS* Cycle 1 and 2. Redder colours indicate the presence of a plateau. The black line points to the zero-age main sequence. Grey dashed lines represent red and blue limits of the instability strip for observed pulsators in the δ Scuti regime (Murphy et al. 2019).

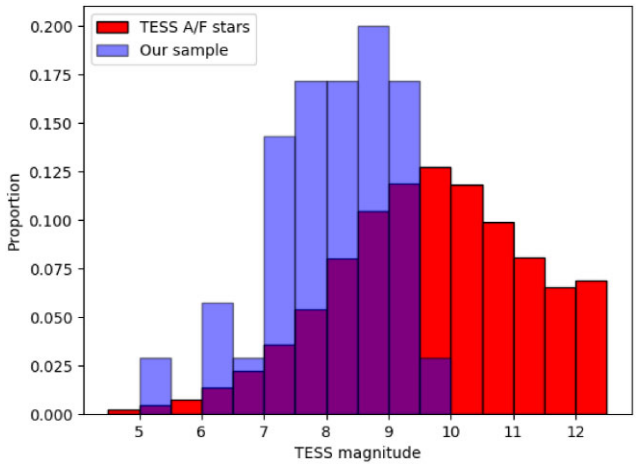

Figure 4. Proportion of *TESS* A/F stars by magnitude (red) compared with our sample of δ Scuti stars (blue; see text).

Then, we selected a homogeneous sample only from *TESS* (Transiting Exoplanet Survey Satellite; Ricker et al. 2015) using all Cycle 1 or 2 sectors. These stars are from, or close to, the northern or southern pole continuous viewing zone. This yields a ∼352-d light curve and a Rayleigh frequency of 33 nHz. The cadence of the studied *TESS* light curves is ∼2 min. Therefore, the Nyquist frequency is 4167 μHz, covering, by far, all the typical frequency regime. Using all available sectors, their duty cycle range between 70 per cent and 85 per cent due to periodic data downlinks and several data anomalies.

Our sample includes stars representative of the δ Scuti frequency regime only. Fig. 3 presents the Hertzsprung–Russell (HR) diagram location of the stars in our sample inside the instability strip. They are colour-coded by the plateau factor we will introduce in Section 4. We discard other kinds of pulsators, such as γ Doradus or roAp stars, that lie in similar regimes. To avoid light contamination from other stars, we also discard both optical pairs and eclipsing binaries.

TESS space telescope observe stars from 5 to 13 mag (see Fig. 4). After the previous selection, our sample includes stars with magnitudes from 5 to 10 mag. Our sample shows cases with and without plateau for each of the most populated magnitudes. We expect to populate all these magnitudes using future *TESS* Cycles or with long observations from PLATO (Rauer et al. 2014).

After their reduction (see Section 3), we provide the analysis of 36 *TESS* light curves some of them previously unstudied (tables O.1–O.36 available online).

3 METHODOLOGY

We employed the δ Scuti Basics Finder pipeline (referred to as δSBF hereafter, see BF2017 and references therein) to characterize the power spectrum structure of δ Scuti stars. The pipeline is based on a nested prewhitening cascade where the cascade is repeated each time reducing spectral window effects by interpolating the gaps using the harmonic model found in the previous prewhitening cascade. Thus, the spectral window is effectively removed by using a K-stage method which consists of K-1 consecutive interpolation stages followed by a final frequency extraction stage. The K-stage method is an improvement of the three-stage method introduced in Barceló Forteza et al. (2015) which allows to fill the gaps of the light curves with a solution that is optimized iteratively at each stage.

Our implementation of the interpolation is aimed to preserve the information that is contained in the segments without gaps while reducing the spectral window convolution effects. In this sense, our pipeline achieves to clear the periodogram from most of the spectral window effects that hamper the frequency estimation of the signal. These effects cannot be efficiently removed with a classical prewhitening method alone (Pascual-Granado et al. 2018). Therefore, while numerical errors for harmonic parameters are the same for frequencies that are not affected by the interferences caused by the spectral window, these can improve considerably for those that are affected. The only hypothesis of this method is that the statistics are the same inside and outside of the gaps, which is reasonable for coherent oscillators.

In the next paragraphs, we will briefly describe the complete algorithm, for an extended description see BF2017.

3.1 Iterative algorithm

The first stage of the K-stage method starts with a linear interpolation of the gaps to obtain an initial data set that can be used to calculate an FFT. In that way, the periodogram allows us to estimate the parameters of the highest peak. Then, sine wave fitting in the gapped light curve is performed using the estimated parameters as initial guess. The sine wave is subtracted from the gapped light curve and then the first stage of the algorithm re-starts with the residuals. This interpolation stage finishes when $S_i < 0$ (see equation 1).

At the end of the first stage, a full solution for the harmonic signal present in the light curve will be found. This solution will be used at the beginning of the second stage to build a harmonic model (equation 2) to interpolate the gaps. Using this non-linear interpolation, the algorithm finds more accurate guesses than in first stage. The rest of the steps are identical to the first stage. In successive stages, the solution will be improved with the new harmonic model based on the parameters of the previous stage.

In the last stage (K-stage), different to the previous ones, we use the interpolated light curve for the sine wave fitting. To be considered valid, all detected peaks must have a signal-to-noise ratio of 4 or higher.

3.2 Efficacy of gap-filling

The efficacy of gap-filling improves with each interpolation stage, benefiting from the availability of more information in the light

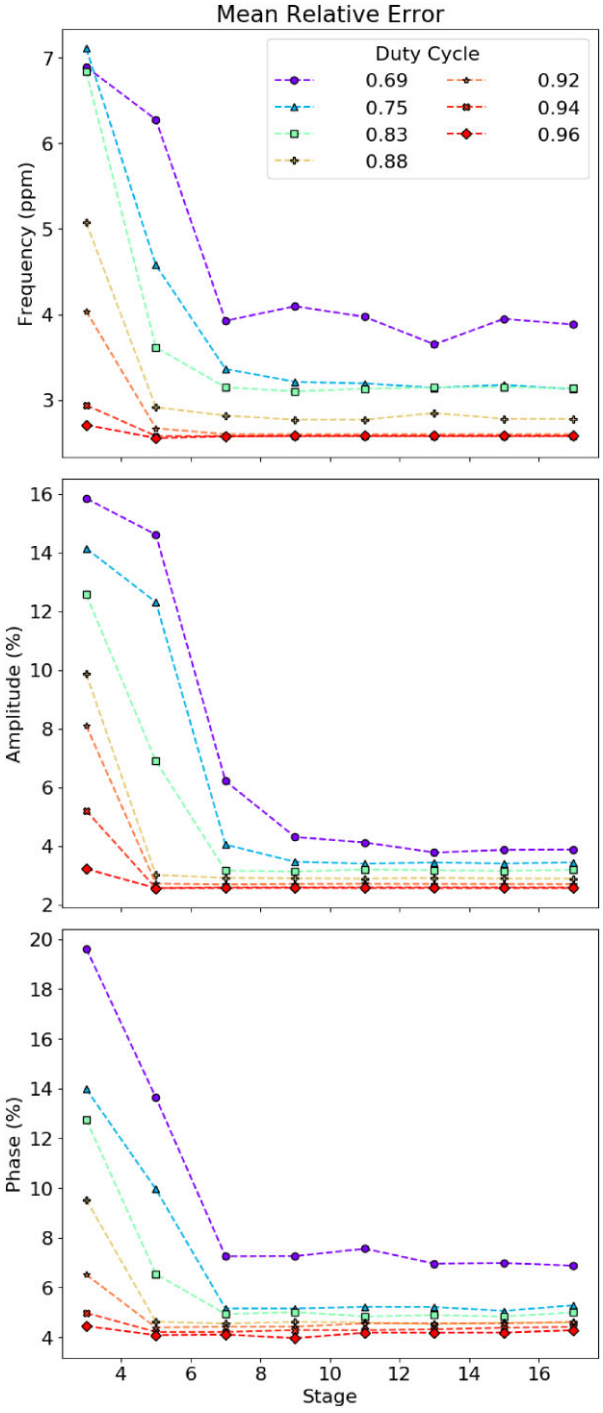

Figure 5. Top panel: Mean relative frequency deviation of detected modes from simulated ones with realistic duty cycles. Mid and bottom panels: Same as top panel but for amplitude and phase, respectively. We emphasize that the frequency deviations are much smaller than those of the amplitude and the phase (ppm instead of %).

curve. This improvement stems from the minimization of errors in the subtracted harmonic parameters after each stage (see Fig. 5). Furthermore, the method's efficiency is augmented by the excellent observational window provided by space missions and the high signal-to-noise ratio (García et al. 2014; Barceló Forteza et al. 2015). For example, the three-stage method effectively minimizes the background noise by up to a factor of 3 for duty cycles of 60 per cent and up to 14 for duty cycles around 90 per cent (Barceló Forteza et al. 2020). Using the K-stage method, we achieve a factor around 10 or higher for all duty cycles (see Appendix A). The background noise is reduced by one order of magnitude.

The high accuracy of the method for frequencies, amplitudes, and phases is shown in Fig. 5 (top, mid, and bottom panels, respectively). We conducted tests using simulated light curves containing approximately 1400 actual δ Scuti star oscillations. These tests incorporated elements such as noise, realistic *TESS* duty cycles, and the presence of gaps. For these thousand of low-amplitude simulated peaks, the mean difference in frequency is up to the nHz in the worst scenario (duty cycle of 69 per cent) using only the original three stages (see top panel in Fig. 5). This is an order of magnitude lower than the Rayleigh frequency. The accuracy increases after each stage until converging to a minimum parameter deviation. For amplitudes, the 4 per cent deviation leads to residuals around 0.4 ppm, far below the detected peaks and the allowed signal-to-noise ratio. The low-amplitude peaks may have a phase deviation between 4 and 5 per cent in the convergence zone for duty cycles of 75 per cent or higher. For duty cycles of 70 per cent, the mean deviation almost doubles its value possibly defining the limit for the study of low-amplitude peaks using interpolation methods. For more details of the benefits using our non-linear interpolation method, see Appendix A.

The results of this test are equivalent to those made in Barceló Forteza et al. (2015) especially for the amplitude. The higher frequency resolution and the sinusoidal cadence also may increase the phase accuracy for *Kepler* light curves.

To validate our method, we also used the deviation from the harmonic model (see equation 2 with $N = 0$) for the high-quality data in the simulated light curves, excluding the points identified as gaps (top panel of Fig. 6). In all cases, the deviation from the harmonic model decreases until reaching a minimum value, distinct from 0 due to the presence of simulated noise. The bottom panel depicts the number of detected peaks per stage. Our results demonstrate that three stages are sufficient for analysing low-amplitude peaks in light curves with high duty cycles ($\gtrsim$90 per cent). In these light curves, the appropriate number of peaks is detected, and the deviation from the harmonic model reaches its minimum at the third stage. For lower duty cycles, additional stages are required to avoid spurious peaks and accurately detect the genuine ones.

In studying our sample of stars, we determine the optimal number of stages that minimize their deviation from the harmonic model. We also consider the minimum stages required based on their duty cycles, as determined through simulations. For these reasons, the required stages to reduce the light curves we consider here are a minimum of seven.

3.3 Signal analysis

After the frequency analysis of each δ Scuti star, we studied the number of peaks and their contribution to the total amount of signal taking into account their signal level ($\log S_i$, see e.g. Fig. 7). We focus on peaks from the envelope ($\log S_i \geq -1$) and those belonging to the grass ($\log S_i \leq -2$). On the one hand, the power spectrum presents a considerably higher percentage of grass peaks than those from the envelope (see top panel in Fig. 7). On the other hand, the contribution to the signal of a single dominant peak ($\log S_i \geq 1$; see bottom panel) is several times bigger than all peaks from grass: a $\sim$15 per cent compared to a $\sim$5 per cent for this particular star.

However, the number of peaks of each regime and their contribution to the signal are different for each star. Fig. 8 shows the typical values of both parameters for the stars of our sample. We

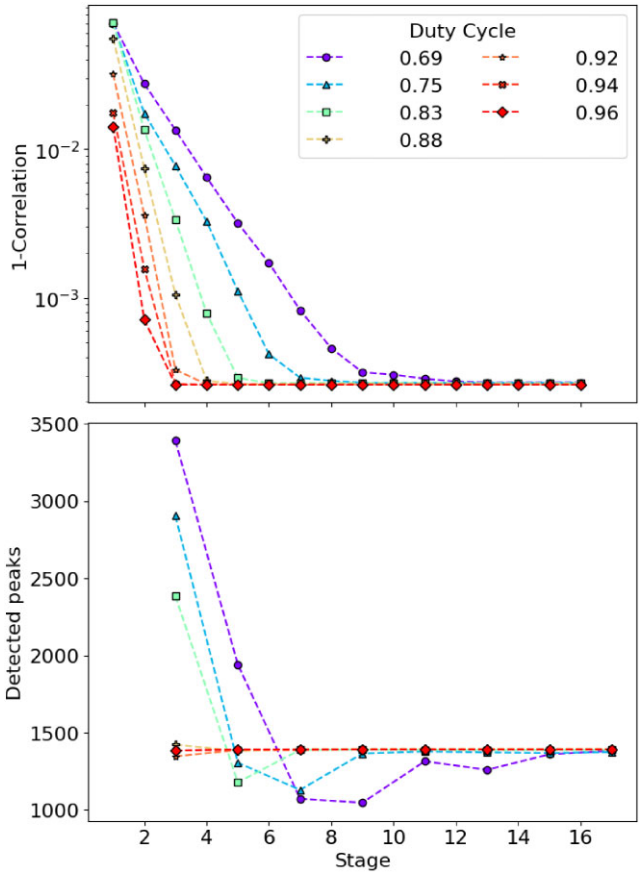

Figure 6. Top panel: Deviation from perfect correlation at each stage between the original and detected harmonic flux for high-quality data points for simulated δ Scuti light curves with different realistic duty cycles. Bottom panel: Number of detected peaks as a function of the number of stages for the same simulations as above panel.

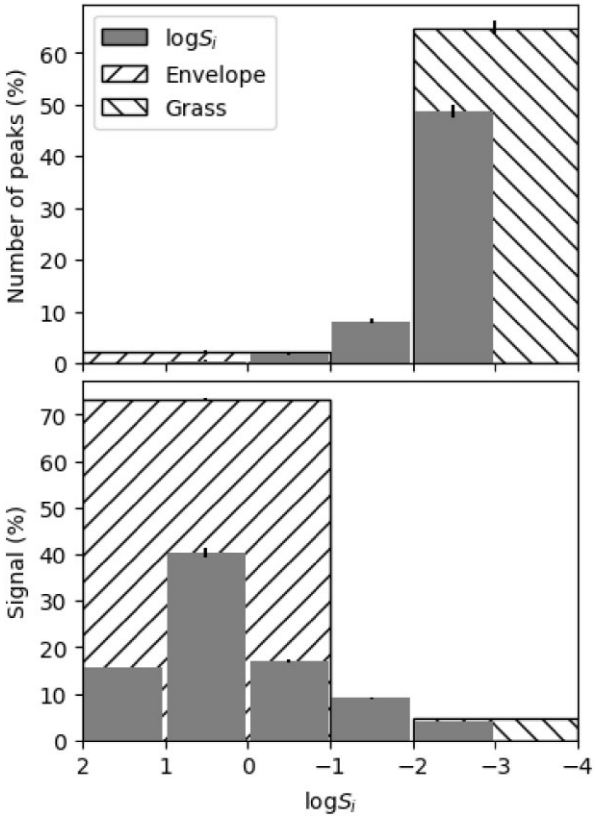

Figure 7. Top panel: Contribution to the number of peaks subtracted from TIC 198 456 033 power spectrum as a function of their signal level. Note the error bars on top of each measurement. Bottom panel: Same as top panel for the contribution to the total amount of signal.

differentiated the stars with and without plateau (grey and beige areas, respectively). The envelope shows no separation between both kinds of power spectra. On the contrary, they are well separated in the grass. We also compared two specific δ Scuti stars with (TIC 230136491; red line) and without a plateau (TIC 259130275; purple line). Both have a similar number of dominant peaks and contribution to the signal but they differ by orders of magnitude at grass level.

4 GRASS PARAMETRIZATION

As in BF2017, we also use δSBF to parametrize the grass by studying the mean amplitude and the mean density of peaks per 10-μHz bin ($A_{\rm bin}$ and $n_{\rm bin}$, see top and bottom panels of Fig. 9, respectively). However, we modify the pipeline in order to characterize and compare all kinds of δ Scuti stars, including hybrids, only measuring their grass properties in the δ Scuti frequency regime (see Section 1). Instead of using the rough limit between γ Doradus and δ Scuti frequency regimes at ∼ 50 μHz, we calculate the frequency at minimum peak density (ν_λ) around the fundamental mode. The density of peaks for δ Scuti stars shows a minimum between g and p modes domain (Moya et al. 2017; see also bottom panels in fig. 9).

We also modified the way we calculate the cut-off frequency. Fig. 9 presents two characteristic cases of grass with and without plateau (TIC 198 456 033 and TIC 232604221, as in Figs 1 and 2, respectively). The left column shows a grass with plateau. As we described in Section 1, in this case the grass manifests a high density of peaks with stable amplitude at frequencies up to the cut-off frequency. For higher frequency peaks up to the higher frequency detected (ν_N), the density of peaks rapidly decreases and their amplitude drops to noise. On the contrary, right column in Fig. 9 shows a grass without plateau, i.e. a low density of grass peaks and an unstable amplitude, including empty bins with no peaks. The grass density decrease after the cut-off frequency is barely noticeable.

Then, to constrain the plateau frequency regime, we measure the cut-off frequency for peak density ($\nu_{c,n}$). At that frequency, the mean density of peaks per bin ($n_{\rm bin}$) decrease below the following threshold:

$$n_{th} = N^{-1}_{\rm bins}(\nu_\lambda, \nu_N) \sum_{\nu_\lambda}^{\nu_N} n_{\rm bin}(\nu) \approx n_g\,, \tag{3}$$

where n_g is the mean density of grass peaks for all the δ Scuti frequency regime and $N(\nu_a, \nu_b)$ is the number of bins between the frequencies. Finally, we measure the mean density of the plateau ($\bar{n}$) using its proper limits,

$$\bar{n} = N^{-1}_{\rm bins}(\nu_\lambda, \nu_{c,n}) \sum_{\nu_\lambda}^{\nu_{c,n}} n_{\rm bin}(\nu)\,. \tag{4}$$

To study in detail these frequency limits for all stars of our sample, see Appendix B.

We have taken a similar approach studying the amplitudes. The cut-off frequency for amplitude ($\nu_{c,A}$) points to the decay of the mean amplitude per bin ($A_{\rm bin}$) below their threshold (A_{th}; analogously to

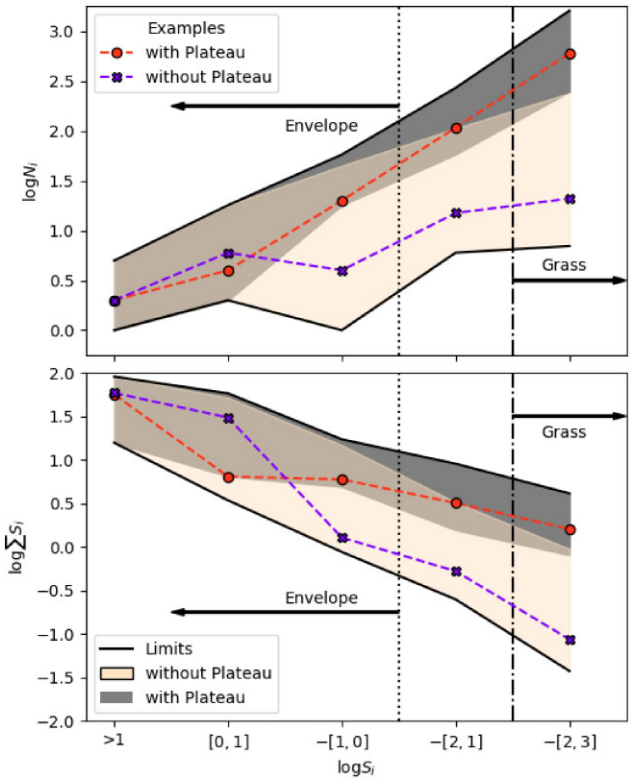

Figure 8. Top panel: Typical number of peaks subtracted from the power spectra for our sample of δ Scuti star at each signal level (from top to bottom solid black lines). Grey and beige areas point to the typical values for cases with and without plateau, respectively. We also included two representative cases (red circles and purple x dashed lines, respectively). Bottom panel: Same as the top panel but for the contribution to the total amount of signal.

equation 3). Since the density of peaks and the amplitude do not have to reach their threshold value at the same frequency, the two cut-off frequencies do not have to be equal (see right panels in Fig. 9). Then, the mean amplitude of the plateau is

$$\bar{A} = N_{\rm bins}^{-1}(\nu_\lambda, \nu_{c,A}) \sum_{\nu_\lambda}^{\nu_{c,A}} A_{\rm bin}(\nu)\,. \tag{5}$$

The stability of the mean amplitude can be used to study the presence or absence of a plateau. Then, we define the plateau factor as

$$\Xi \equiv 1 - N_{\rm bins}^{-1}(\nu_\lambda, \nu_{c,n}) \sum_{\nu_\lambda}^{\nu_{c,n}} \left| 1 - \frac{A_{\rm bin}(\nu)}{\bar{A}} \right|\,. \tag{6}$$

The higher the plateau factor, the more similar the grass to a boxcar function. We also visually note this relation by comparing the power spectra for the two stars discussed previously with high and low plateau factors (left and right columns in Fig. 10, respectively). Each panel of Fig. 10 shows the power spectral structure of the original light curve, and also after subtracting a consecutive signal level down to the detection limit. These two stars have a similar number of peaks in the envelope but TIC 198 456 033 has one order of magnitude more peaks in the grass forming the plateau (see second panels from bottom). In addition to the sparse grass peaks of TIC 232604221, their amplitudes are far from stable. Moreover, TIC 198 456 033 presents a power excess in the δ Scuti frequency regime at the detection limit compared with noise (see bottom panel of Fig. 10). On the contrary, TIC 232 604 221 lacks of this power excess once the detection limit is reached.

We repeat this exercise for all stars of our sample. Taking into account the peaks at each signal level, Fig. 11 shows a random distribution regarding the presence of plateau ($\Xi \to 1$) at each signal level of the envelope. Nevertheless, this distribution is organized between signal levels $-1 \geq \log S_i \geq -2$ and remains down to the detection limit. The higher the grass contribution, the higher the plateau factor. In fact, all cases with $\Xi \gtrsim 0.64$ show a grass with plateau (grey area in Fig. 11). This distribution suggests that the limits between grass and envelope properly separate both power spectral structures and the mechanisms for the plateau emergence should be further explored.

4.1 With(out) plateau

The definition of the plateau factor is not related with the density of grass peaks but with their mean amplitude throughout the pulsation regime. However, we find that the higher the mean density of plateau peaks, the higher the plateau factor (see Fig. 12). In fact, we can differentiate two grass regimes:

$$\Xi = \begin{cases} 0.634(4)\bar{n} - (12 \pm 2)10^{-3}, & \bar{n} \lesssim 1.01 \pm 0.01 \\ 0.03566(3)\bar{n} + 0.5815(3), & \bar{n} \gtrsim 1.01 \pm 0.01\,; \end{cases} \tag{7}$$

where the Pearson correlation coefficient for each regime is $r\sim 0.903$ and $r\sim 0.869$, respectively. For the sparse grass regime, the plateau factor rapidly increases with $\bar{n}$ up to a saturation limit ($\Xi_s \sim 0.62 \pm 0.02$). On the contrary, the dense grass regime slightly increases with $\bar{n}$. This limit is in agreement with the observed plateau for all δ Scuti stars with $\Xi \gtrsim 0.64$ (see Fig. 11).

The grass density decay,

$$\Delta n = \bar{n} - n_g\,, \tag{8}$$

also presents these two regimes (see Fig. 13). For power spectra at the sparse grass regime ($\Xi \lesssim 0.6$), the grass density decay is close to zero. This is coherent with the absence of plateau $\bar{n} \sim n_g$. On the contrary, the decay significantly increases after the saturation limit,

$$\Delta n = \begin{cases} 0.14 \pm 0.11, & \Xi \lesssim 0.62 \pm 0.02\,; \\ (13.0 \pm 2.9)\Xi + (7.7 \pm 1.4), & \Xi \gtrsim 0.62 \pm 0.02\,; \end{cases} \tag{9}$$

where $r\sim 0.897$. δ Scuti stars at the dense grass regime ($\Xi \gtrsim 0.6$) show a significantly higher density of grass peaks within the frequency regime $\nu \in [\nu_\lambda, \nu_{c,n}]$ than outside.

Regarding the amplitudes, Fig. 14 shows how the plateau mean amplitude distribution appears to be completely random. The signal-to-noise ratio of the low-amplitude structure is around 4 or higher for all cases except for seven δ Scuti stars at the sparse grass regime. Therefore, most of them can be considered as significant structures. Nevertheless, these structures in the sparse grass regime cannot be called plateau, they are only a dispersed significant peaks.

Finally, our results, compiled in Table 1, are in agreement with the qualitative study of the low-amplitude part of the power spectra for δ Scuti stars: there are stars with and without plateau. The plateau factor allows us to quantitatively characterize the power spectra but separates these two regimes thanks to its saturation value: $\Xi_s \sim 0.60 \pm 0.02$. The power spectra at the sparse grass regime do not have enough density of grass peaks to create a plateau. However, power spectra at the dense grass regime have a high density of peaks, with a significant decay towards high frequencies, allowing us to observe the plateau.

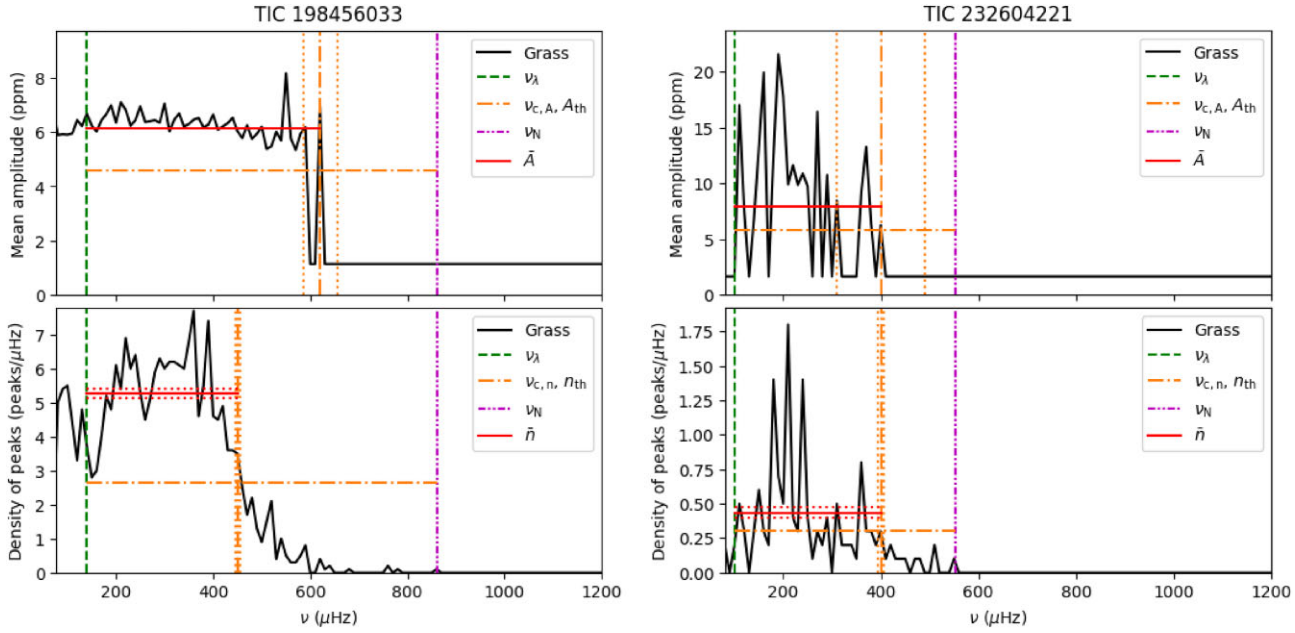

Figure 9. Grass parametrization for TIC 198 456 033 and TIC 232 604 221 (left and right columns, respectively). Top panels: Mean amplitude of grass peaks per 10-μHz bin (black solid) compared with the mean amplitude of the plateau ($\bar{A}$; red solid) from the frequency at minimum peak density (ν_λ; green dashed) to the cut-off frequency for amplitude ($\nu_{c,A}$; dash–dotted orange). The amplitude threshold is also represented (A_{th}; dash–dotted orange). Bottom panels: Mean density of grass peaks per 10-μHz bin (black solid) and the mean density of plateau peaks ($\bar{n}$; red solid) between the frequency at minimum peak density (dashed green) and the cut-off frequency for peak density ($\nu_{c,n}$; dash–dotted orange). The density threshold is also represented (n_{th}; dash–dotted orange).

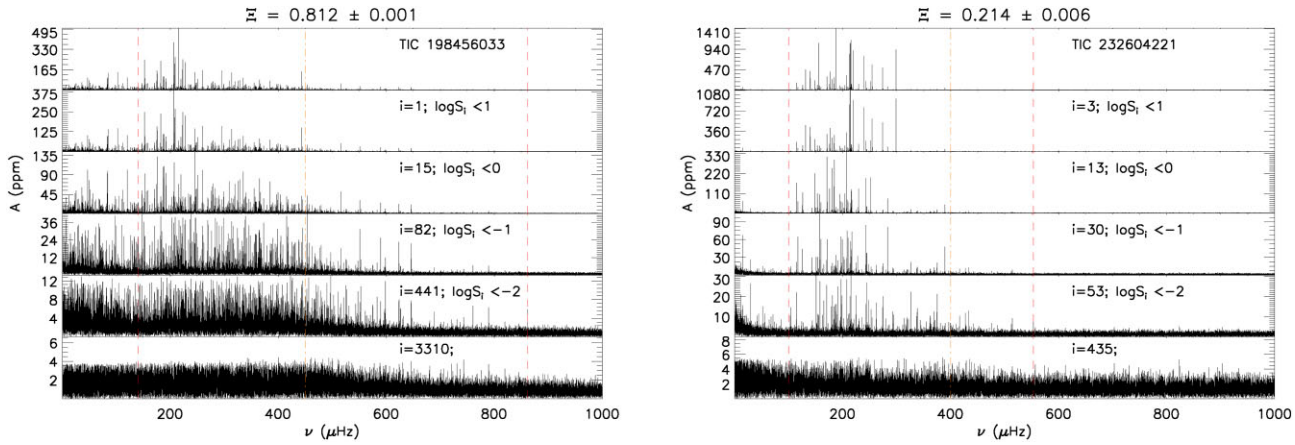

Figure 10. From top to bottom: Original power-spectral structure for TIC 198 456 033 (left) and TIC 232 604 221 (right column), and also those after extracting consecutive signal levels, i.e. the indicated number of peaks. The second panel from the bottom shows the grass level and the presence or absence of a plateau (Ξ, see text). Red dashed lines point to ν_λ and the highest detected frequency (ν_N). Orange dash–dotted line points to the cut-off frequency ($\nu_{c,n}$).

5 DISCUSSION

After having characterized the behaviour of the low-amplitude power spectra of δ Scuti stars, studying the differences between members belonging to each regime may help us to find the mechanism for the emergence of the plateau.

We noted that stars with same magnitudes show both high and low plateau factor values (see top panel in Fig. 15). Mid panel of Fig. 15 shows higher values of the mean density of plateau peaks than the saturation limit for some δ Scuti stars. These values are randomly distributed in regard to their apparent magnitude. A similar behaviour is observed for the grass density decay in the bottom panel. Consequently, despite the lack of statistics outside *TESS* magnitude 7–10, we can argue that the apparent magnitude is not the mechanism behind the plateau characteristics. In any case, the relations of the sparse and dense grass regimes should be followed when all the grass peaks are significantly higher than noise.

At this point, we can rule out the possibility of a cascade bug as the main cause of the plateau. An important key point is the window effect correction. Low-duty-cycle light curves should be properly interpolated or the low-amplitude peaks should not be studied (see Fig. 6). Using our methodology, we recover non-spurious peaks only ($S_i > 0$). Moreover, we noted that TIC 198 456 033 and TIC 232 604 221 have the same duty cycle (83.8 per cent) but they are cases of power spectra with and without plateau, respectively. However, the higher number of peaks, the higher number of errors should produce the prewhitening method (Balona 2014). The typical number of genuine peaks of the envelope is around a few tens

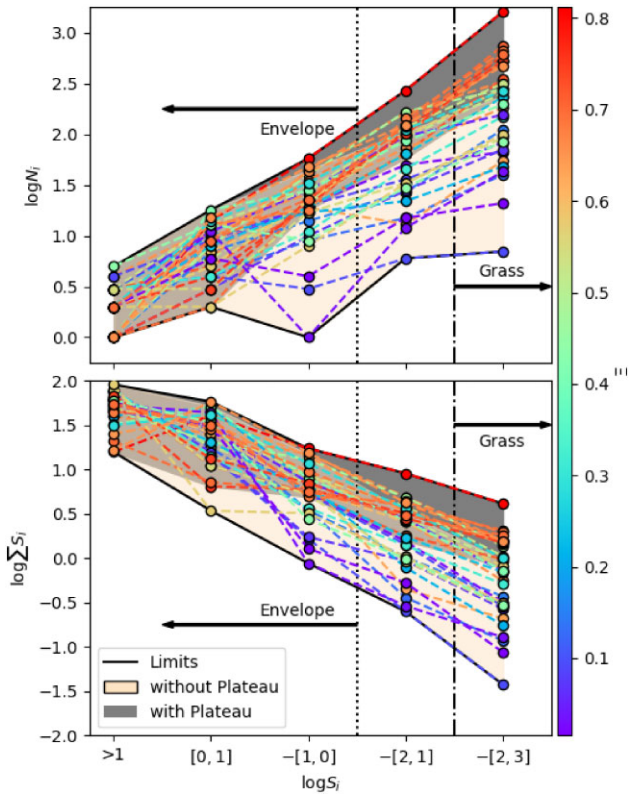

Figure 11. Top panel: Number of peaks subtracted from the power spectrum of each δ Scuti star with regard to their signal level. Bottom panel: Same as the top panel for the contribution to the total amount of signal. Redder colours indicate a higher plateau factor (Ξ, see Section 4). As in Fig. 8, the grey (beige) area indicates a grass with(out) plateau.

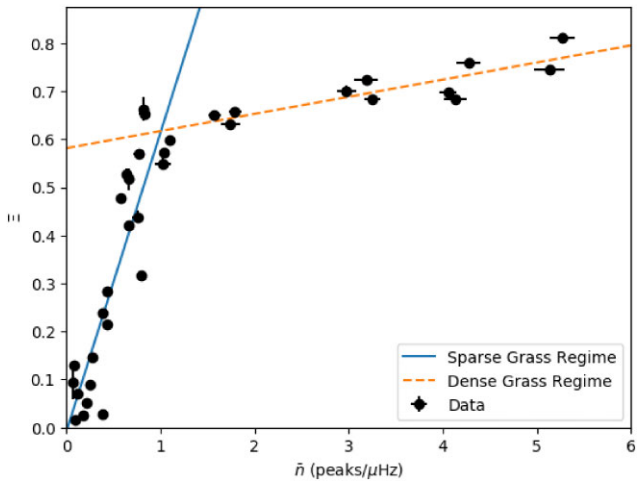

Figure 12. Plateau factor with the mean density of plateau peaks (black points). The plateau factor follows two different relations depending on the regime: the sparse grass regime (solid blue line) and the dense grass regime (dashed orange line).

(Barceló Forteza et al. 2018). This is in agreement with number of envelope peaks for our sample for any Ξ (log $N_i \sim 1.5$, see Fig. 11). Since there is no relation between the number of envelope peaks and the presence of a plateau, a cascade bug due to consecutive errors in the analysis should not be the main cause of the presence of a plateau. Oppositely, the non-harmonic nature of the signal referred

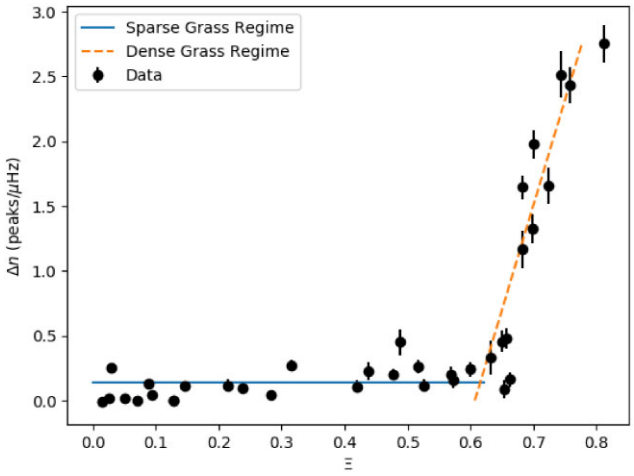

Figure 13. Grass density decay versus the plateau factor. Solid blue (dashed orange) line represents the relation between both parameters at sparse (dense) grass regime.

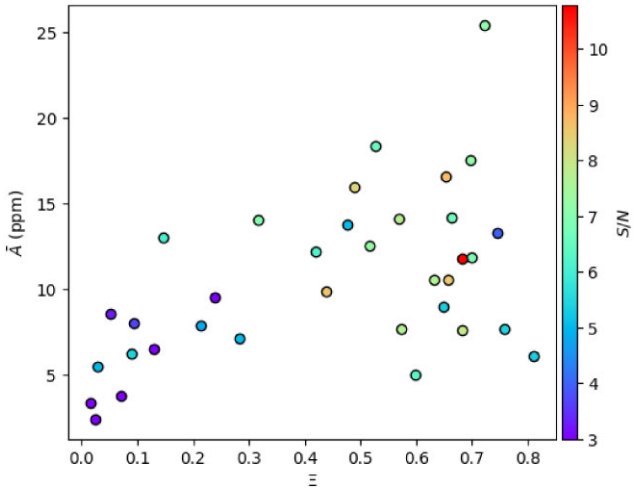

Figure 14. Mean amplitude of the plateau versus the plateau factor. The colour points to the signal-to-noise ratio.

by Pascual-Granado et al. (2015) and Suárez et al. (2020) might originate non-spurious peaks so fractality cannot be discarded as a plausible cause for the plateau. In fact, de Franciscis et al. (2018) found that a fractal fingerprint may be present in the light curves of some δ Scuti stars.

5.1 Selection and amplitude modulation mechanisms

The observed distribution of modes may be in agreement with the predicted instability of low-amplitude high-degree modes in addition to a few low-degree ones (Daszyńska-Daszkiewicz et al. 2006). The amplitudes of each different degree modes depend on the disc-averaging factor:

$$A_\ell \propto b_{\ell,\lambda} = \int_0^1 \mu h_\lambda P_\ell(\mu)\, d\mu\,, \tag{10}$$

where $P_\ell(\mu)$ are the Legendre polynomials and h_λ is the limb-darkening law (e.g. Claret 1998, 2017). Comparing the amplitudes of the highest envelope peak and the mean amplitude of the grass, we calculated the expected grass degree for each star, $\ell_{\rm grass}$, between

Table 1. Grass parameters measured for our sample of δ Scuti stars. Second and third columns are the effective temperature and luminosity by Stassun et al. (2019), respectively. The following columns are all defined in Section 4. Fourth, fifth, and sixth columns are the frequency at minimum peak density, the cut-off frequency for peak density, and the highest frequency detected, respectively. The seventh and eighth columns are the mean amplitude of the plateau and the plateau factor, i.e. the stability of the plateau. The ninth and tenth columns are the mean density of the plateau peaks and the grass density decay, respectively. Last column indicates the grass regime. A more complete version of this Table has been included in the Online Only Material adding HD catalogue number, spectral type, metallicity ([Fe/H]), projected velocity (vsin i), and remarks from the Simbad catalogue.

TIC	$T_{\rm eff}$ (K)	L ($L_\odot$)	ν_λ (μHz)	$\nu_{\rm c,n}$ (μHz)	$\nu_{\rm N}$ (μHz)	$\bar{A}$ (ppm)	Ξ	$\bar{n}$ (peaks/μHz)	Δn (peaks/μHz)	Grass regime
25117273	7170 ± 140	10.4 ± 0.5	100 ± 5	980 ± 5	986.546	6.5 ± 1.5	0.129 ± 0.003	0.08 ± 0.01	0.00 ± 0.01	Sparse
33732017	7950 ± 140	16.7 ± 0.7	160 ± 5	480 ± 10	738.988	12.5 ± 0.8	0.517 ± 0.022	0.66 ± 0.05	0.26 ± 0.05	Sparse
38570985	7750 ± 150	13.0 ± 0.5	130 ± 10	510 ± 5	626.006	14.2 ± 0.6	0.663 ± 0.024	0.82 ± 0.05	0.16 ± 0.06	Saturation point
150441810	7390 ± 130	28 ± 5	90 ± 5	290 ± 5	546.894	25.4 ± 1.1	0.723 ± 0.002	3.19 ± 0.13	1.66 ± 0.14	Dense
160602772	7110 ± 130	10.2 ± 0.9	90 ± 5	370 ± 5	437.576	16.6 ± 0.5	0.654 ± 0.006	0.83 ± 0.05	0.09 ± 0.07	Saturation point
176931266	7550 ± 130	10.2 ± 0.4	110 ± 5	480 ± 5	901.671	6.2 ± 0.8	0.089 ± 0.009	0.25 ± 0.03	0.13 ± 0.03	Sparse
198456033	8360 ± 120	30.7 ± 1.4	140 ± 5	450 ± 5	861.473	6.11 ± 0.14	0.812 ± 0.001	5.27 ± 0.13	2.75 ± 0.14	Dense
198478755	6910 ± 120	13.8 ± 0.6	90 ± 10	140 ± 5	272.704	8 ± 6	0.10 ± 0.04	0.07 ± 0.04	0.04 ± 0.04	Sparse
199573174	7200 ± 120	9.5 ± 0.4	100 ± 10	–	180.973	–	–	–	–	No grass detected
219863247	7450 ± 130	10.7 ± 0.4	110 ± 5	540 ± 5	874.430	13.0 ± 1.3	0.147 ± 0.001	0.273 ± 0.025	0.11 ± 0.03	Sparse
220411786	7590 ± 140	16.1 ± 0.7	140 ± 5	450 ± 5	503.268	2.4 ± 0.5	0.025 ± 0.004	0.181 ± 0.024	0.01 ± 0.03	Sparse
229473905	7660 ± 130	11.0 ± 0.3	110 ± 5	680 ± 5	683.355	3.8 ± 0.8	0.070 ± 0.003	0.122 ± 0.015	0.00 ± 0.02	Sparse
229676244	7210 ± 120	22.0 ± 0.9	70 ± 5	240 ± 5	307.561	10.5 ± 0.4	0.632 ± 0.003	1.74 ± 0.10	0.33 ± 0.13	Dense
230136491	8650 ± 130	21.5 ± 1.0	140 ± 5	400 ± 5	792.089	7.7 ± 0.4	0.758 ± 0.001	4.27 ± 0.13	2.43 ± 0.14	Dense
232604221	7250 ± 130	13.2 ± 0.5	100 ± 5	400 ± 5	553.060	7.9 ± 1.1	0.214 ± 0.006	0.4 ± 0.04	0.12 ± 0.05	Sparse
232606431	7830 ± 110	9.1 ± 0.2	140 ± 5	690 ± 5	916.651	4.96 ± 0.25	0.599 ± 0.002	1.10 ± 0.05	0.24 ± 0.06	Saturation point
233580734	7910 ± 130	13.8 ± 0.5	160 ± 10	450 ± 25	1097.316	11.8 ± 0.6	0.700 ± 0.011	2.97 ± 0.10	1.97 ± 0.11	Dense
233627515	8370 ± 130	13.3 ± 0.7	160 ± 5	570 ± 5	876.738	13.8 ± 0.9	0.477 ± 0.006	0.58 ± 0.04	0.20 ± 0.04	Sparse
235709086	7600 ± 140	19.9 ± 0.9	150 ± 5	620 ± 5	735.728	7.7 ± 0.3	0.573 ± 0.001	1.04 ± 0.05	0.15 ± 0.06	Saturation point
237104803	8300 ± 130	18.7 ± 0.9	140 ± 5	830 ± 5	1207.349	14.0 ± 1.0	0.316 ± 0.004	0.80 ± 0.04	0.27 ± 0.04	Sparse
237214784	7810 ± 150	6.5 ± 0.3	130 ± 5	830 ± 5	921.516	8.5 ± 1.0	0.051 ± 0.001	0.213 ± 0.017	0.01 ± 0.02	Sparse
256458460	7820 ± 170	8.3 ± 0.5	120 ± 5	740 ± 5	973.901	9.5 ± 0.7	0.239 ± 0.001	0.384 ± 0.025	0.10 ± 0.03	Sparse
258773721	7940 ± 120	12.3 ± 0.4	130 ± 5	460 ± 5	618.751	9.0 ± 0.3	0.649 ± 0.003	1.57 ± 0.07	0.45 ± 0.08	Dense
259101798	7600 ± 200	9.5 ± 0.8	80 ± 5	560 ± 5	703.640	18.3 ± 0.8	0.527 ± 0.011	0.64 ± 0.04	0.12 ± 0.05	Sparse
259130275	7210 ± 130	9.3 ± 0.4	130 ± 10	360 ± 5	363.090	3.3 ± 0.9	0.015 ± 0.007	0.088 ± 0.019	0.01 ± 0.03	Sparse
269663477	7170 ± 140	15.9 ± 0.9	96 ± 5	230 ± 5	448.904	15.9 ± 1.6	0.569 ± 0.011	1.03 ± 0.09	0.45 ± 0.10	Sparse
280068700	7650 ± 120	12.3 ± 0.3	130 ± 5	410 ± 5	551.136	14.1 ± 0.8	0.569 ± 0.006	0.77 ± 0.05	0.20 ± 0.06	Sparse
287151185	7530 ± 120	9.0 ± 0.3	80 ± 5	550 ± 5	672.778	12.2 ± 0.7	0.420 ± 0.011	0.67 ± 0.04	0.11 ± 0.05	Sparse
293936044	7870 ± 140	19.3 ± 0.7	140 ± 5	440 ± 5	617.432	11.73 ± 0.24	0.683 ± 0.003	4.13 ± 0.12	1.17 ± 0.14	Dense
298782588	7690 ± 130	32.3 ± 0.9	90 ± 5	410 ± 5	1075.366	5.5 ± 1.0	0.029 ± 0.001	0.39 ± 0.04	0.25 ± 0.04	Sparse
300329283	8470 ± 130	13.9 ± 0.6	190 ± 5	650 ± 5	1173.346	7.58 ± 0.23	0.683 ± 0.003	3.25 ± 0.09	1.64 ± 0.09	Dense
348843152	8480 ± 150	33.1 ± 1.9	100 ± 5	300 ± 5	545.601	13.3 ± 0.5	0.745 ± 0.007	5.13 ± 0.16	2.51 ± 0.18	Dense
350559515	7270 ± 140	14.8 ± 0.7	80 ± 5	290 ± 5	445.513	9.8 ± 1.1	0.438 ± 0.013	0.76 ± 0.06	0.23 ± 0.07	Sparse
391927456	7840 ± 150	9.4 ± 0.4	120 ± 5	730 ± 5	816.841	7.1 ± 0.5	0.283 ± 0.003	0.432 ± 0.027	0.05 ± 0.04	Sparse
416401395	8060 ± 130	15.3 ± 0.7	160 ± 5	620 ± 5	907.640	17.5 ± 0.5	0.698 ± 0.001	4.06 ± 0.09	1.33 ± 0.11	Dense
441762590	7780 ± 130	10.9 ± 0.2	120 ± 5	540 ± 5	748.984	10.6 ± 0.6	0.657 ± 0.001	1.79 ± 0.07	0.48 ± 0.08	Dense

6 and 14. However, for high-degree modes, the geometric term $(\ell - 1)(\ell + 2)$ has to be taken into account (Balona & Dziembowski 1999). For these cases, the geometric term partially compensates for the $b_{\ell,\lambda}$ decrease with ℓ due to limb-darkening (we assume the non-linear law of Claret 2017). This decrease can scale as $\ell^{-3.5}$ (Dziembowski 1977), thus, the amplitude follows $\ell^{-1.5}$ and the expected grass degree increases. Fig. 16 shows the values of expected grass degree for each star compared with the plateau factor, the mean density of the plateau peaks, and the grass density decay (top, mid, and bottom panels respectively). The $\ell_{\rm grass}$ of our sample ranges from 18 to 76 but we find no dependence with any of the plateau characteristic parameters. Therefore, we do not discard the pulsating nature of the grass peaks as these may be high-degree modes, but another mechanism would then be required to explain the emergence of the plateau.

The mode selection mechanism should be further studied star by star. Using multicolour photometry, the degree identification of the mode is feasible (e.g. Garrido 2000; Daszyńska-Daszkiewicz et al. 2003, 2021) and our results may be tested, strengthening the need for colour information from future space missions. However, other effects should be taken into account. Non-linearities may modify the characteristics of the selected peaks, including frequency, amplitude, and phase modulation with time (e.g. Breger & Montgomery 2014; Lares-Martiz 2022).

The maximum density of peaks reached in our sample ($n_{\rm max} \sim 9.6 \pm 0.4$ peaks/μHz) implies one peak each 100 nHz, approximately three times the Rayleigh frequency of our light curves ($\nu_R \sim 33$ nHz). Although this is not a guarantee for the absence of unresolved peaks due to period or amplitude variations, their presence has been minimized thanks to our strategy (see Section 2). δ Scuti stars may have cyclic variations from months to years (e.g. Barceló Forteza et al. 2015; Bowman et al. 2016) and the stars of our sample are not an exception (Barceló Forteza et al., in preparation). BF2017 suggests mode variation as one of the main causes of the presence of the plateau apart from rotation. In fact, both phenomena may be related in different ways such as resonant coupling (Goupil et al. 2000). The departure from exact splitting for moderate rotation rates may produce mode variations. For faster and faster rotation rates, the resonant condition is lost, even the high-order perturbation theories are no longer valid: this happens at about 0.35 of the break-up frequency (Ω_K), that is $v_{\rm eq} \gtrsim 150$ km s^{-1} (Soufi et al. 1998; Ballot, Lignières & Reese 2013). It is also the rotation rate at which high-degree chaotic modes appear in the stellar oscillation spectra (Lignières et al. 2006).

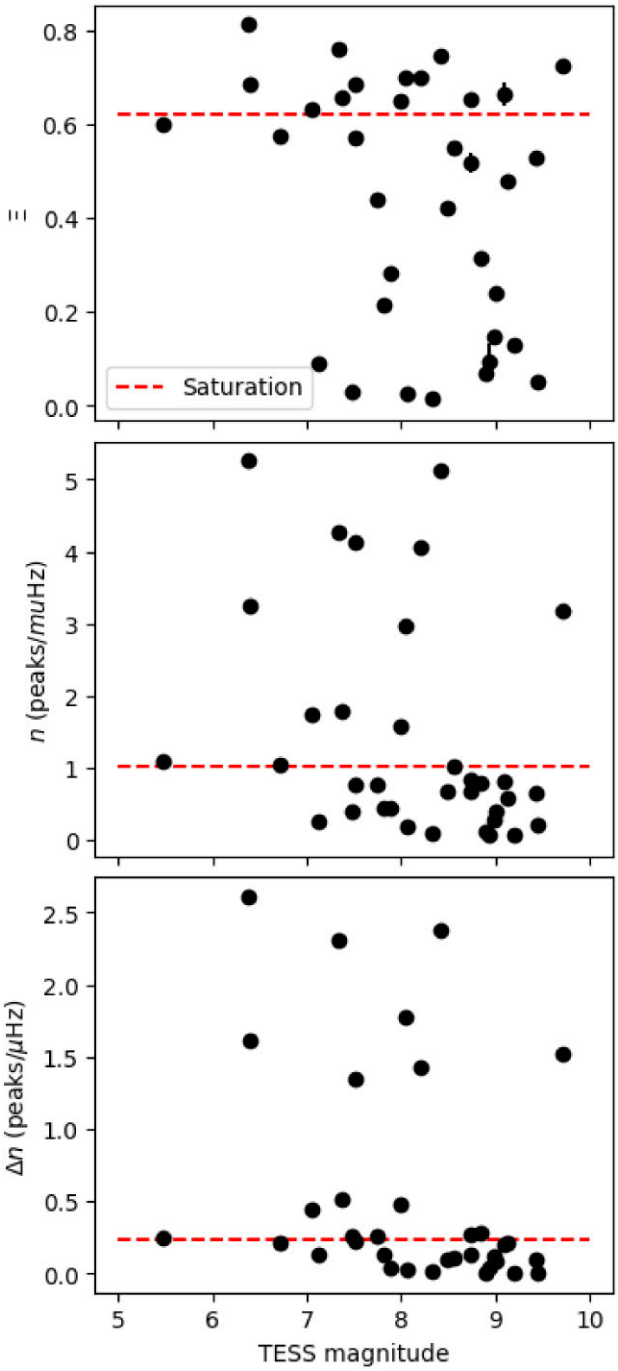

Figure 15. From top to bottom: Plateau factor, mean density of the plateau peaks, and the grass density decay versus *TESS* magnitude for the stars of our sample. Red dashed lines point to their respective saturation limit values between the sparse and dense grass regimes (see Section 4.1 and Figs 12 and 13).

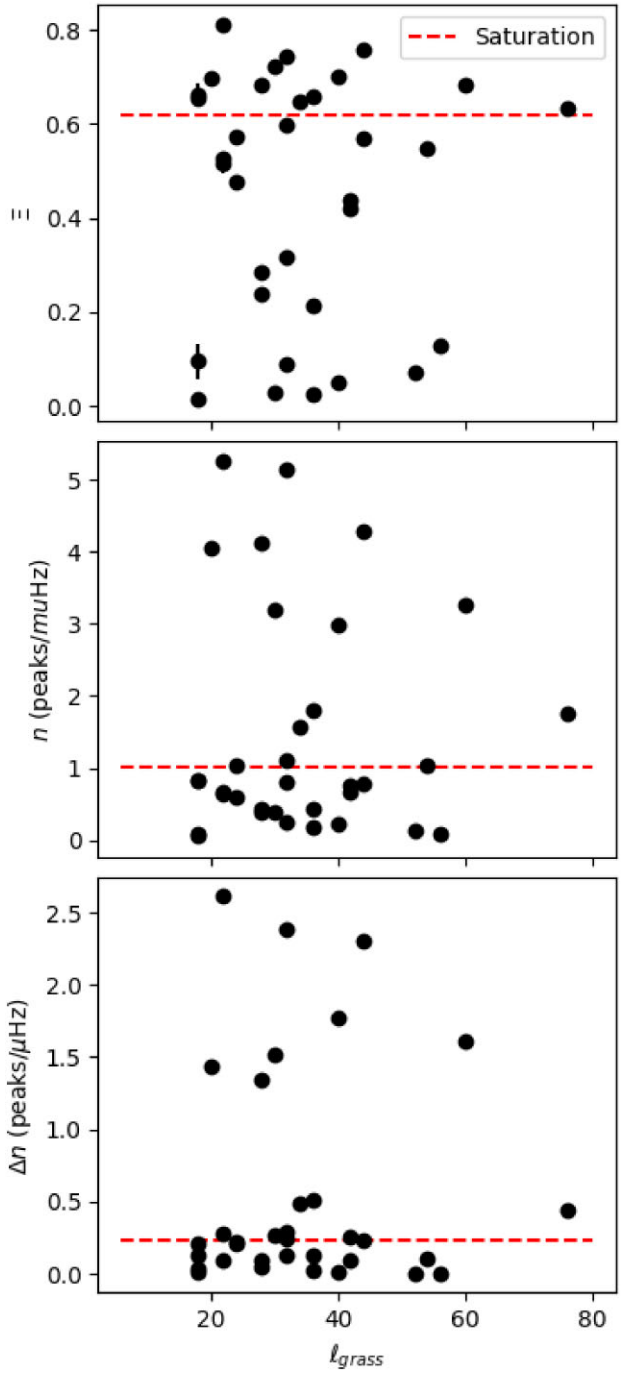

Figure 16. The same parameters as in Fig. 15 but for the expected grass degree, $\ell_{\rm grass}$.

5.2 Down to the background

The statistical model used to estimate the background noise and therefore the detection of significant peaks in the power spectrum, depend on hypotheses about the physical properties of the star. Noise may not only include white noise but other frequency-dependent components such as those produced by activity or granulation (Harvey 1985). The observation of this stochastic motion requires a convective surface such as in Sun-like stars (Michel et al. 2008) and red giants (Kallinger et al. 2010). Kallinger & Matthews (2010) highlight that early A stars may have a thin, but non-negligible, convective layer in their surfaces. They suggest granulation as the cause of the high amount of low-amplitude peaks, including a threshold to stop the prewhitening and avoid them. However, they use a linear interpolation method that may artificially change the distribution of frequencies (Pascual-Granado et al. 2018). On the contrary, we use our non-linear interpolation method to fill the gaps achieving a significant background noise reduction (see Section 3). In addition, we use a local signal-to-noise ratio and therefore we take into account the background noise variation with frequency.

Furthermore, the false alarm probability should take into account the fractal component of the light curve (de Franciscis et al. 2019), thus, redefining the classical detection limit of harmonic signal. The application of this technique for the study of the grass will be the focus of future work.

In any case, our study does not rule out granulation as a mechanism for plateau formation. One possibility may be the coupling of rotation and convection. Rotation may extend a subsurface convective zone, mainly on the equator but also at the poles (Maeder, Georgy & Meynet 2008). Then, fast-rotating stars may have larger stochastic contributions than slow rotators. Moreover, their characteristics may change depending on the inclination from the line of sight.

5.3 Rotation, ageing, and grass regimes

As we introduced in Section 1 and discussed above in Section 5, the rotation rate may be the main cause of the presence of a plateau. There might be not an unique mechanism related with rotation, but different flavours such as the convection–rotation connection (Maeder et al. 2008), the pulsation–rotation coupling (e.g. Buchler et al. 1997), or the emergence of chaotic modes due to the flattening of the star (e.g. Lignières & Georgeot 2009; Evano, Lignières & Georgeot 2019; Mirouh 2022). BF2017 suggested rotation rate as one of the mechanisms behind the presence of the plateau. In fact, they found that the higher their rotation rate, the higher their peak density. Taking into account their results, all stars in the dense grass regime should be fast rotators, and the saturation point may indicate the emergence of the chaotic modes (Barceló Forteza et al., in preparation). Furthermore, the visibility of modes in a flattened star depends on its inclination (e.g. Reese et al. 2013, 2017), which can explain the seemingly random distribution of the mean amplitude of the plateau (see Fig. 14).

Age may also play a significant role. δ Scuti stars are located in the HR diagram from the main sequence to the giant branch (see Fig. 3). During the evolution process, the stellar parameters such as radius, temperature, or luminosity, and the internal structure change with time (e.g. Pamyatnykh 2000). Therefore, the power spectra of this kind of stars also change (Breger 1998; Christensen-Dalsgaard 2000) and, consequently, their seismic indices such as the large separation ($\Delta\nu$; e.g. García Hernández et al. 2015, 2017; Mirouh et al. 2019; Bedding et al. 2020), the frequency at maximum power ($\nu_{\max}$; e.g. Barceló Forteza et al. 2018, 2020; Hasanzadeh et al. 2021), or the splitting due to rotation (s; e.g. BF2017; Ramón-Ballesta et al. 2021; Reese et al. 2021).

Stellar rotation on the main sequence depends on the angular momentum loss and redistribution at the formation phases of the star (e.g. Sun et al. 2021). Once the initial rotation rate at the zero-age main sequence (ZAMS; $t/t_{\rm MS} \sim 0$) has been established, the rotation evolution up to the terminal-age main sequence ($t/t_{\rm MS} \sim 1$) can be described taking into account the physics of the star. δ Scuti stars increase their rotation rate with respect to its break-up frequency (Ω/Ω_K) from ZAMS to $t/t_{\rm MS} \sim 0.4$ and then remain high for the rest of the main sequence (Zorec & Royer 2012). Similarly, Georgy et al. (2013) models show an increase of the rotation rate from $t/t_{\rm MS} \sim 0.1$ to 0.9. The higher the initial Ω/Ω_K, the greater its increase. For both cases, this growth is mainly due to the decrease of break-up frequency (Ω_K), i.e. there is a lower contribution of the gravity force against the centrifugal force.

$$\Omega/\Omega_K \propto \Omega \left(\frac{R^3}{GM}\right)^{1/2} = \sqrt{\frac{\Omega^2 R}{g_{\rm eff}}}. \quad (11)$$

Taking into account the Ω_K variation with age, one δ Scuti star at the sparse grass regime may increase Ω/Ω_K and, consequently, its density of peaks. Therefore, a δ Scuti star may change from a sparse grass regime to a dense grass regime, especially for these stars with intermediate to fast initial rotation close to the transition between both regimes.

6 CONCLUSIONS

The low-amplitude power spectra of δ Scuti stars contains crucial information. It can present a constant-amplitude power excess known as plateau, or not. Both cases are of interest. This structure can be described by a high density of low-amplitude peaks between two characteristic frequencies: the frequency at minimum peak density (ν_λ), that separates the γ Doradus and δ Scuti pulsation regimes; and the cut-off frequency that is the high-frequency limit where the density of peaks drops ($\nu_{c,n}$).

The plateau can be quantitatively studied thanks to the low-amplitude, low-signal peaks known as grass ($\log S_i \leq -2$). There are two regimes depending on the density of these kind of peaks ($\bar{n}$) and the stability of their amplitudes (Ξ). In the sparse grass regime, the grass is not dense enough and its amplitude not uniform enough to make a plateau. On the contrary, in the dense grass regime, the high density of grass peaks with similar amplitude allows us to observe the plateau.

The saturation point ($\Xi_s \sim 0.6$) is reached at 1 grass peak per μHz, approximately. At that point, the grass density decay increases from 0.23 up to 2.75 peaks/μHz for our sample. Including more *TESS* Cycles or light curves from PLATO may allow us to observe denser plateaus and refine the saturation point. In any case, the plateau is always significant in the dense grass regime, but its mean amplitude is not correlated with the density of peaks nor the plateau factor.

Unlike the grass, there are no significant differences in the high-signal peaks of the envelope ($\log S_i \geq -1$) for cases with and without plateau. As BF2017 suggested, the power spectra of δ Scuti stars appear to have two different structures: the envelope formed by stellar pulsations and the grass which origin still in debate. The amplitude differences between both structures suggest a grass made by high-degree modes in contrast to low-degree modes of the envelope. Space-based light curves and the K-stage interpolation method make it possible to properly observe and interpret these low-amplitude peaks with enough signal-to-noise ratio.

After having parametrized the behaviour of the grass for δ Scuti stars, studying the stellar structure of each component should be our next step. The differences between members belonging to each regime may help us to find the mechanism for the emergence of the plateau.

Here, we discard most of the non-physical explanations apart from the possibly fractal nature of the signal. On the contrary, one of the most appealing candidates is stellar rotation. The saturation point may be related to the emergence of chaotic modes due to the flattening of the star at high rotation rates. Furthermore, rotation may be related to most of the other mechanisms such as mode coupling or granulation. All these possibilities deserve to be explored by looking for rotational signatures at the power spectra such as rotational split modes or surface rotation signals.

ACKNOWLEDGEMENTS

The authors want to thank the referee for all comments and suggestions which have definitely allowed us to significantly improve the manuscript. We also wish to thank the *TESS* team whose

efforts made these results possible. Funding for the *TESS* mission is provided by the NASA Explorer Program. SBF, JCS, AGH, and GMM received financial support from the Spanish State Research Agency (AEI) projects no. PID2019-107061GB-C64: 'Contribution of the UGR to the PLATO2.0 space mission. Phases C/D-1'. SBF, JPG, and GMM acknowledge financial support from the Severo Ochoa grant CEX2021-001131-S funded by MCIN/AEI/10.13039/501100011033. SBF also thanks the resources received from 'Planes Complementarios' Astrophysics and High Energy Physics of the Spanish MCIU (AST22_00001_26) and also these from the PLATO project collaboration with Centro de Astrobiología (PID2019-107061GB-C61). JPG acknowledges financial support from project PID2019-107061GB-C63 from the 'Programas Estatales de Generación de Conocimiento y Fortalecimiento Científico y Tecnológico del Sistema de I+D+i y de I+D + i Orientada a los Retos de la Sociedad'. AGH acknowledges funding support from 'European Regional Development Fund/Junta de Andalucía-Consejería de Economía y Conocimiento' under project E-FQM-041-UGR18 by Universidad de Granada. GMM acknowledges financial support from the project AST22_00001_8 of the 'Junta de Andalucía and the Ministerio de Ciencia, Innovación y Universidades' funded by the NextGenerationEU and the 'Plan de Recuperación, Transformación y Resiliencia'. MLM gratefully acknowledges support from NSF grants AST-1910396 and AST-2108975 and NASA grants 80NSSC22K0622, 80NSSC21K0245, and NNX16AB76G.

DATA AVAILABILITY

The original light curves can be obtained from MAST *TESS* Bulk Downloads. The results of the frequency analysis and grass characterization are available at CDS via anonymous ftp to cdsarc.u-strasbg.fr (130.79.128.5) or via https://cdsarc.cds.unistra.fr/viz-bin/cat/J/MNRAS/535/2189.

REFERENCES

Antoci V. et al., 2014, ApJ, 796, 118
Baglin A., Auvergne M., Barge P., Deleuil M., Catala C., Michel E., Weiss W., COROT Team, 2006, in Fridlund M., Baglin A., Lochard J., Conroy L., eds, ESA SP-1306: The CoRoT Mission Pre-Launch Status - Stellar Seismology and Planet Finding. ESA, Noordwijk, p. 33
Ballot J., Lignières F., Reese D. R., 2013, in Goupil M., Belkacem K., Neiner C., Lignières F., Green J. J., eds, Lecture Notes in Physics, Vol. 865, Studying Stellar Rotation and Convection. Springer-Verlag. Berlin, p. 91
Balona L. A., 2011, MNRAS, 415, 1691
Balona L. A., 2014, MNRAS, 439, 3453
Balona L. A., Dziembowski W. A., 1999, MNRAS, 309, 221
Balona L. A., Dziembowski W. A., 2011, MNRAS, 417, 591
Barceló Forteza S., Michel E., Roca Cortés T., García R. A., 2015, A&A, 579, A133
Barceló Forteza S., Roca Cortés T., García Hernández A., García R. A., 2017, A&A, 601, A57
Barceló Forteza S., Roca Cortés T., García R. A., 2018, A&A, 614, A46
Barceló Forteza S., Moya A., Barrado D., Solano E., Martín-Ruiz S., Suárez J. C., García Hernández A., 2020, A&A, 638, A59
Bedding T. R. et al., 2020, Nature, 581, 147
Borucki W. J. et al., 2010, Science, 327, 977
Bowman D. M., Kurtz D. W., 2018, MNRAS, 476, 3169
Bowman D. M., Kurtz D. W., Breger M., Murphy S. J., Holdsworth D. L., 2016, MNRAS, 460, 1970
Breger M., 1998, in Deubner F.-L., Christensen-Dalsgaard J., Kurtz D., eds, Proc. IAU Symp. 185, New Eyes to See Inside the Sun and Stars. Kluwer, Dordrecht, p. 323
Breger M., 2000, in Breger M., Montgomery M., eds, ASP Conf. Ser. Vol. 210, Delta Scuti and Related Stars. Astron. Soc. Pac., San Francisco, p. 3
Breger M., Montgomery M. H., 2014, ApJ, 783, 89
Buchler J. R., Goupil M.-J., Hansen C. J., 1997, A&A, 321, 159
Chevalier C., 1971, A&A, 14, 24
Christensen-Dalsgaard J., 2000, in Breger M., Montgomery M., eds, ASP Conf. Ser. Vol. 210, Delta Scuti and Related Stars. Astron. Soc. Pac., San Francisco, p. 187
Claret A., 1998, A&AS, 131, 395
Claret A., 2017, A&A, 600, A30
Daszyńska-Daszkiewicz J., Dziembowski W. A., Pamyatnykh A. A., 2003, A&A, 407, 999
Daszyńska-Daszkiewicz J., Dziembowski W. A., Pamyatnykh A. A., 2006, Mem. Soc. Astron. Ital., 77, 113
Daszyńska-Daszkiewicz J., Pamyatnykh A. A., Walczak P., Handler G., Pigulski A., Szewczuk W., 2021, MNRAS, 505, 88
de Franciscis S., Pascual-Granado J., Suárez J. C., García Hernández A., Garrido R., 2018, MNRAS, 481, 4637
de Franciscis S., Pascual-Granado J., Suárez J. C., García Hernández A., Garrido R., Lares-Martiz M., Rodón J. R., 2019, MNRAS, 487, 4457
Dziembowski W., 1977, Acta Astron., 27, 203
Evano B., Lignières F., Georgeot B., 2019, A&A, 631, A140
García Hernández A., Martín-Ruiz S., Monteiro M. J. P. F. G., Suárez J. C., Reese D. R., Pascual-Granado J., Garrido R., 2015, ApJ, 811, L29
García Hernández A. et al., 2017, MNRAS, 471, L140
García R. A. et al., 2014, A&A, 568, A10
Garrido R., 2000, in Breger M., Montgomery M., eds, ASP Conf. Ser. Vol. 210, Delta Scuti and Related Stars. Astron. Soc. Pac., San Francisco, p. 67
Georgy C., Ekström S., Granada A., Meynet G., Mowlavi N., Eggenberger P., Maeder A., 2013, A&A, 553, A24
Goode P. R., Thompson M. J., 1992, ApJ, 395, 307
Goupil M.-J., Dziembowski W. A., Pamyatnykh A. A., Talon S., 2000, in Breger M., Montgomery M., eds, ASP Conf. Ser. Vol. 210, Delta Scuti and Related Stars. Astron. Soc. Pac., San Francisco, p. 267
Harvey J., 1985, in Rolfe E., Battrick B., eds, ESA SP-235: Future Missions in Solar, Heliospheric and Space Plasma Physics. ESA, Noordwijk, p. 199
Hasanzadeh A., Safari H., Ghasemi H., 2021, MNRAS, 505, 1476
Kallinger T., Matthews J. M., 2010, ApJ, 711, L35
Kallinger T. et al., 2010, A&A, 509, A77
Kennelly E. J. et al., 1998, ApJ, 495, 440
Kurtz D. W., Hubrig S., González J. F., van Wyk F., Martinez P., 2008, MNRAS, 386, 1750
Lares-Martiz M., 2022, Front. Astron. Space Sci., 9, 932499
Lignières F., Georgeot B., 2009, A&A, 500, 1173
Lignières F., Vidal S., Georgeot B., Reese D., 2006, in Barret D., Casoli F., Lagache G., Lecavelier A., Pagani L., eds, SF2A-2006: Semaine de l'Astrophysique Francaise. p. 479
Maeder A., Georgy C., Meynet G., 2008, A&A, 479, L37
Michel E. et al., 2008, Science, 322, 558
Mirouh G. M., 2022, Front. Astron. Space Sci., 9, 952296
Mirouh G. M., Angelou G. C., Reese D. R., Costa G., 2019, MNRAS, 483, L28
Moskalik P., 1985, Acta Astron., 35, 229
Moya A., Suárez J. C., García Hernández A., Mendoza M. A., 2017, MNRAS, 471, 2491
Murphy S. J., Shibahashi H., Kurtz D. W., 2013, MNRAS, 430, 2986
Murphy S. J., Hey D., Van Reeth T., Bedding T. R., 2019, MNRAS, 485, 2380
Neiner C., Wade G. A., Sikora J., 2017, MNRAS, 468, L46
Nowakowski R. M., 2005, Acta Astron., 55, 1
Pamyatnykh A. A., 2000, in Breger M., Montgomery M., eds, ASP Conf. Ser. Vol. 210, Delta Scuti and Related Stars. Astron. Soc. Pac., San Francisco, p. 215,
Pascual-Granado J., Garrido R., Suárez J. C., 2015, A&A, 581, A89
Pascual-Granado J., Suárez J. C., Garrido R., Moya A., García Hernández A., Rodón J. R., Lares-Martiz M., 2018, A&A, 614, A40

Poretti E. et al., 2009, A&A, 506, 85
Ramón-Ballesta A., García Hernández A., Suárez J. C., Rodón J. R., Pascual-Granado J., Garrido R., 2021, MNRAS, 505, 6217
Rauer H. et al., 2014, Exp. Astron., 38, 249
Reese D. R., Lignières F., Ballot J., Prat V., Barban C., van't Veer-Menneret C., MacGregor K. B., 2013, in Shibahashi H., Lynas-Gray A. E., eds, ASP Conf. Ser. Vol. 479, Progress in Physics of the Sun and Stars: A New Era in Helio- and Asteroseismology. Astron. Soc. Pac., San Francisco, p. 545
Reese D. R., Lignières F., Ballot J., Dupret M.-A., Barban C., van't Veer-Menneret C., MacGregor K. B., 2017, A&A, 601, A130
Reese D. R., Mirouh G. M., Espinosa Lara F., Rieutord M., Putigny B., 2021, A&A, 645, A46
Ricker G. R. et al., 2015, J. Astron. Telesc. Instrum. Syst., 1, 014003
Royer F., Zorec J., Gómez A. E., 2007, A&A, 463, 671
Shibahashi H., Kurtz D. W., 2012, MNRAS, 422, 738
Soufi F., Goupil M. J., Dziembowski W. A., 1998, A&A, 334, 911
Stassun K. G. et al., 2019, AJ, 158, 138
Suárez J. C., Hernández A. G., Moya A., Rodrigo C., Solano E., Garrido R., Rodón J. R., 2014, in Guzik J. A., Chaplin W. J., Handler G., Pigulski A., eds, Proc. IAU Symp. 301, Precision Asteroseismology. Kluwer, Dordrecht, p. 89
Suárez J. C., Garrido R., Pascual-Granado J., García Hernández A., de Franciscis S., Lares-Martiz M., Rodón J. R., 2020, Front. Astron. Space Sci., 7, 12
Sun W., Duan X.-W., Deng L., de Grijs R., 2021, ApJ, 921, 145
Uytterhoeven K. et al., 2011, A&A, 534, A125
Xiong D. R., Deng L., Zhang C., Wang K., 2016, MNRAS, 457, 3163
Zorec J., Royer F., 2012, A&A, 537, A120
Zwintz K. et al., 2020, A&A, 643, A110

SUPPORTING INFORMATION

Supplementary data are available at *MNRAS* online.

Table 1. Grass parameters measured for our sample of δ Scuti stars.

Please note: Oxford University Press is not responsible for the content or functionality of any supporting materials supplied by the authors. Any queries (other than missing material) should be directed to the corresponding author for the article.

APPENDIX A: BENEFITS OF THE K-STAGE METHOD

Our methodology interpolates the light curve with information extracted from the original light curve assuming that missing data is coherent with the original data. Not filling the gaps produces an altered window in the power spectra generating spurious peaks and increasing the background noise (see Figs A1 and A2).

Several examples of the improvement of our analysis are shown in Fig. A1. Comparing the ideal case of a simulated spectrum without noise and the cases with gaps, linear interpolation, and non-linear interpolation (top, mid, and bottom panels, respectively), we noted that non-linear interpolation allows us to find peaks that were below noise level previously to our interpolation (A marks), discard spurious peaks (B marks), and improve the accuracy of all mode parameters (C marks).

The use of linear interpolation alone may be insufficient although it allows to make faster the calculations using, for example, the fast Fourier transform. However, we use the non-linear interpolation and the iterative sine wave fitting to subtract the guess parameters and improve the interpolation stage after stage (see Section 3). The information each wave carries is already at the original light curve. We are not adding new information, we are removing the spectral window effects. To prove it, we make simulated light curves with realistic δ Scuti pulsations and noise. We also simulated them with different realistic *TESS* duty cycles from 70 per cent to 85 per cent. To fulfill all duty cycle cases up to 96 per cent, a random data selection was used to increase the number of high-quality points. Fig. A2 shows how our methodology minimizes the background, comparing the resulting power spectrum with the spectrum of the light curve with gaps. We can also compare them with the linear interpolation. Stage after stage, the background noise is lower until a convergence limit is reached. The improvement is more evident for light curves with lower duty cycles that need more stages to converge (left panel in Fig. A2).

To quantify this improvement, we calculate the background minimization factor:

$$\mathrm{BMF} = \frac{\langle \mathrm{A}(\nu)_{\mathrm{original}} \rangle}{\langle \mathrm{A}(\nu)_{\mathrm{interpolated}} \rangle}, \nu \in [1200 - 1400]\ \mu\mathrm{Hz}; \quad \text{(A1)}$$

where the mean background noise $\langle \mathrm{A}(\nu) \rangle$ is calculated taking into account the power spectra between 1200 and 1400 μHz, where no oscillations are expected. The BMF values after each stage for all considered duty cycles are represented in Fig. A3. We note the aforementioned convergence at stage 7 (see Section 3.2). However, low-duty-cycle light curves require more stages to analyse the proper number of peaks. In any case, we show the K-stage method can minimize an entire order of magnitude the background noise (BMF$\gtrsim$10).

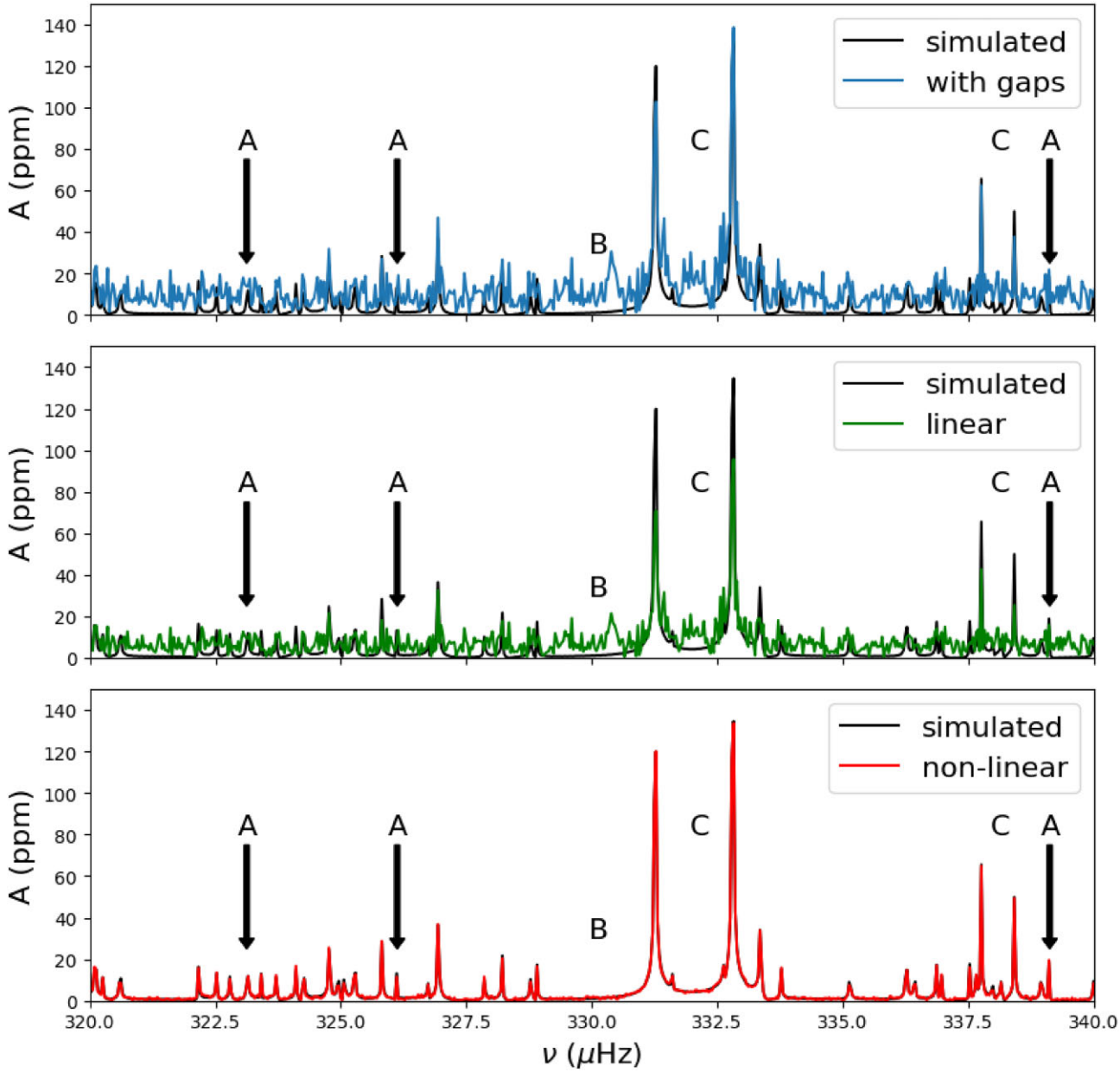

Figure A1. From top to bottom: Comparison between the power spectrum of the simulated light curve (black) and those of the cases with gaps (blue), linear (green), and non-linear interpolation (red), respectively. Arrows and marks point out the main differences between these power spectra (see text).

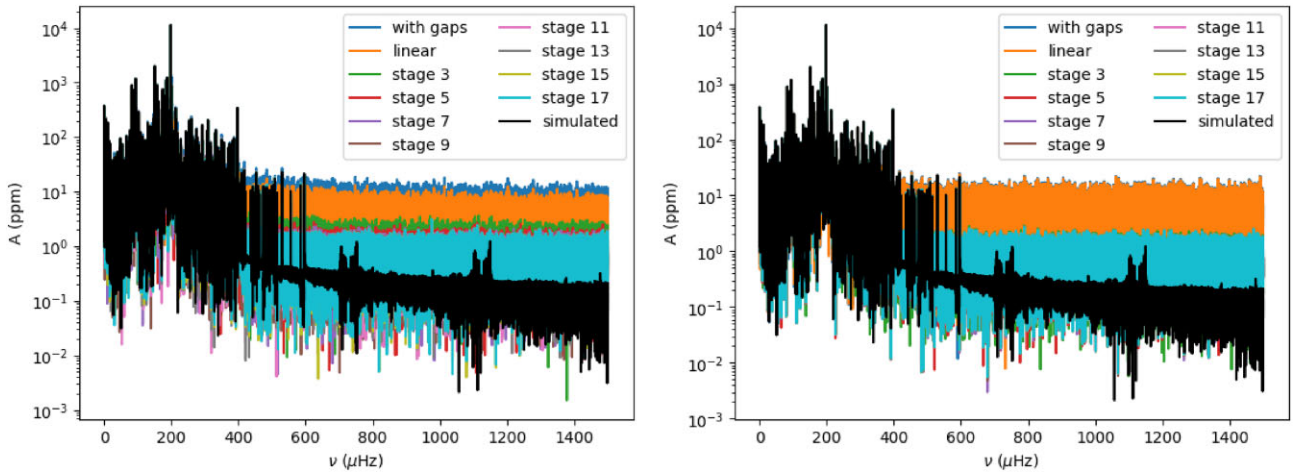

Figure A2. Comparison between the power spectrum of the simulated light curve (black) and these including gaps (blue) with duty cycles of 69 per cent (left) and 95 per cent (right panel), respectively. We included the power spectra after linear interpolation (orange) and also after successive stages of non-linear interpolation.

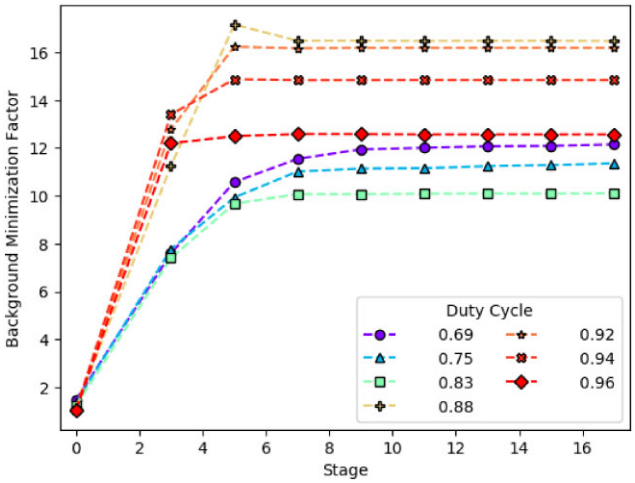

Figure A3. The background minimization factor for each stage of our non-linear interpolation method. Each colour/mark represent a certain duty cycle.

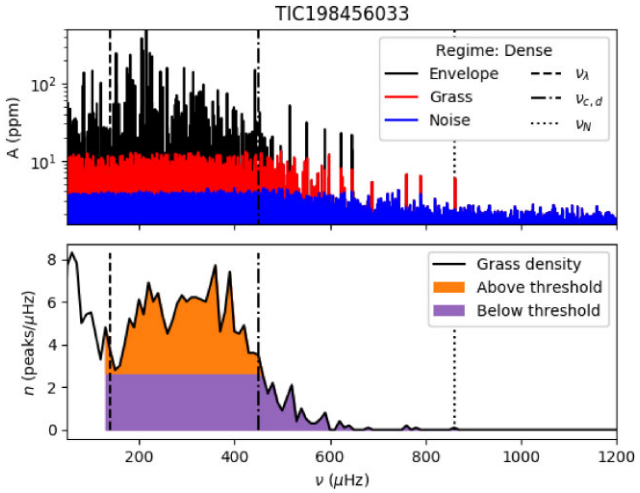

Figure B1. Top panel: Power spectrum of TIC 198456033 (black) including the highlighted grass (red) and noise (blue). Bottom panel: Peak density per 10 μHz chunk (solid black line). The regions above (below) the threshold have been highlighted in orange (purple). The frequency limits have been represented in all panels (see text).

APPENDIX B: FREQUENCY LIMITS OF OUR SAMPLE

Most of the stars of our sample have grass but not all of them have a plateau (see Section 1 and Table 1). We characterize the plateau within its limits, the frequency at minimum peak density (ν_λ), and the cut-off frequency ($\nu_{c,d}$, see Section 4). Both are related with the density of grass peaks, but not with the peaks of the envelope (see Figs B1–B4). In fact, the cut-off frequency indicates the frequency where the grass density decay below the threshold (equation 3). The plateau only appears if the decay is significant compared with the density of peaks up to the maximum frequency peak of the power spectrum (ν_N)

As an example, the top panel in Fig. B1 shows the power spectrum of TIC 198456033, a δ Scuti star in the dense grass regime. The grass has been highlighted in red and differentiated from noise (blue). As expected, the frequency at minimum peak density and the cut-off frequency do not limit the zone were grass appears. However, the number of grass peaks outside the plateau is lower and down to zero after ν_N. Bottom panel shows the peak density versus the frequency. From the frequency at minimum peak density to the cut-off frequency, the density of peaks is higher than the threshold (red). However, after the cut-off frequency the density never rises above its value and also downs to zero after ν_N (blue).

The cut-off frequency defines the plateau for the stars that lie in the dense grass regime (see Section 4.1). However, it also allows us to describe the grass for the stars at the sparse grass regime (e.g. TIC 232604221, see Fig. B2). The peak density also falls below the threshold after $\nu_{c,d}$ and do not rises again. However, the main difference is that their decay is non-significant ($\Delta n \lesssim 0.2$ peaks/μHz) and their amplitudes are not flat enough ($\Xi \lesssim 0.6$, see Table 1). There also are several stars lying in between both regimes at the saturation point ($\bar{n} \sim 1$ peaks/μHz). One example is the case of TIC 160602772 represented in Fig. B3.

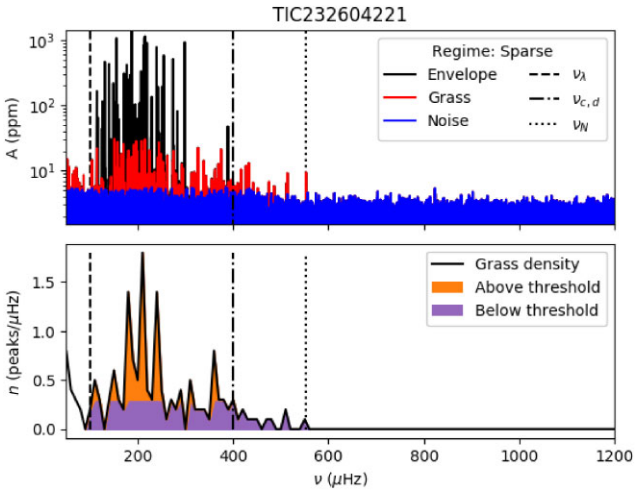

Figure B2. Same as Fig. B1 but for TIC 232604221.

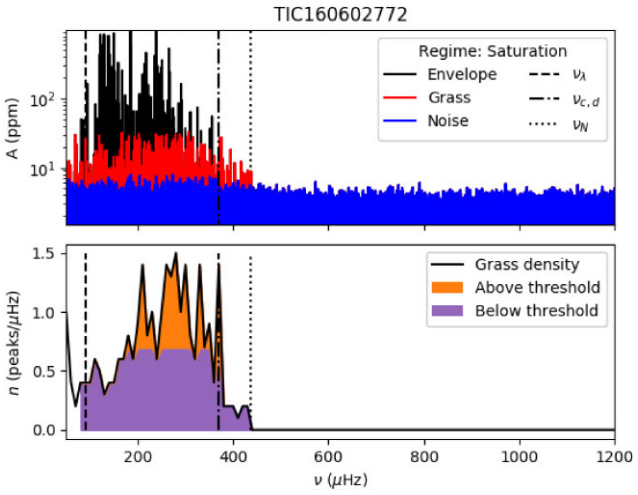

Figure B3. Same as Fig. B1 but for TIC 160602772.

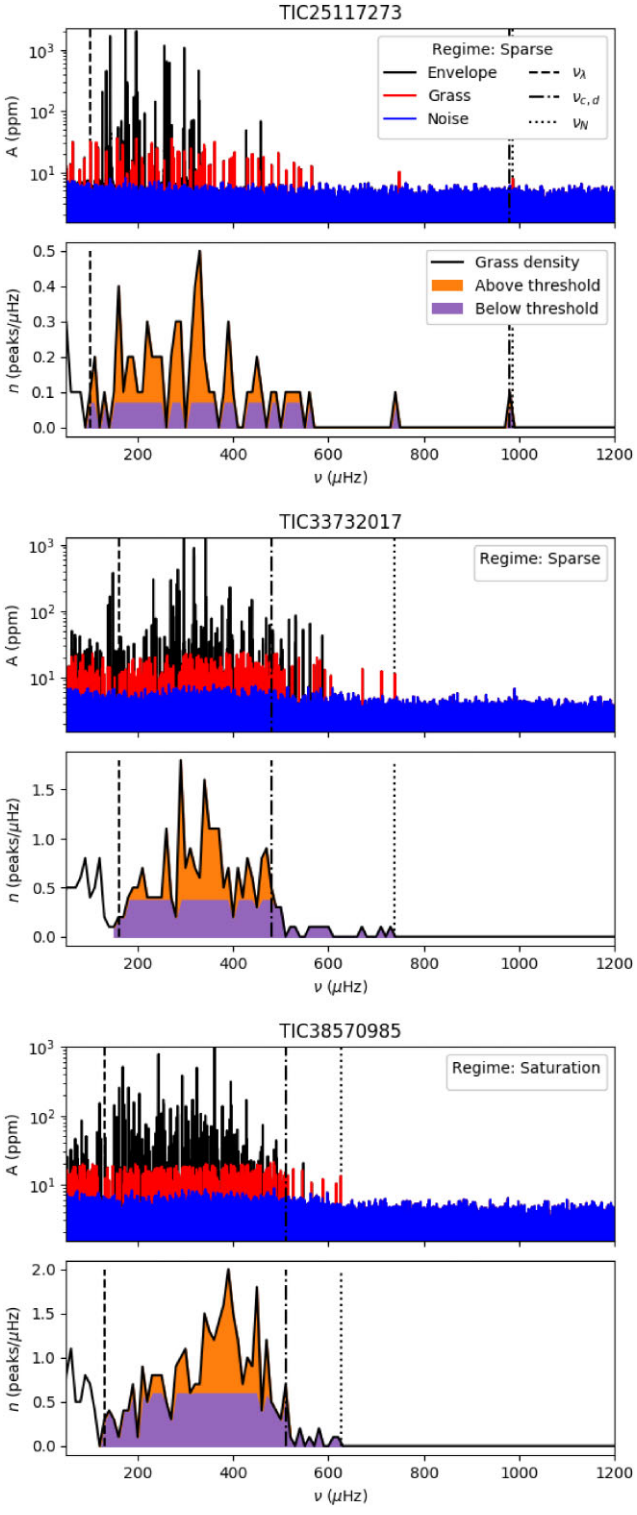

Figure B4. Each two consecutive panels show the power spectrum (top) and the grass peak density (bottom) of one δ Scuti star. The identification number (TIC) for each star is indicated.

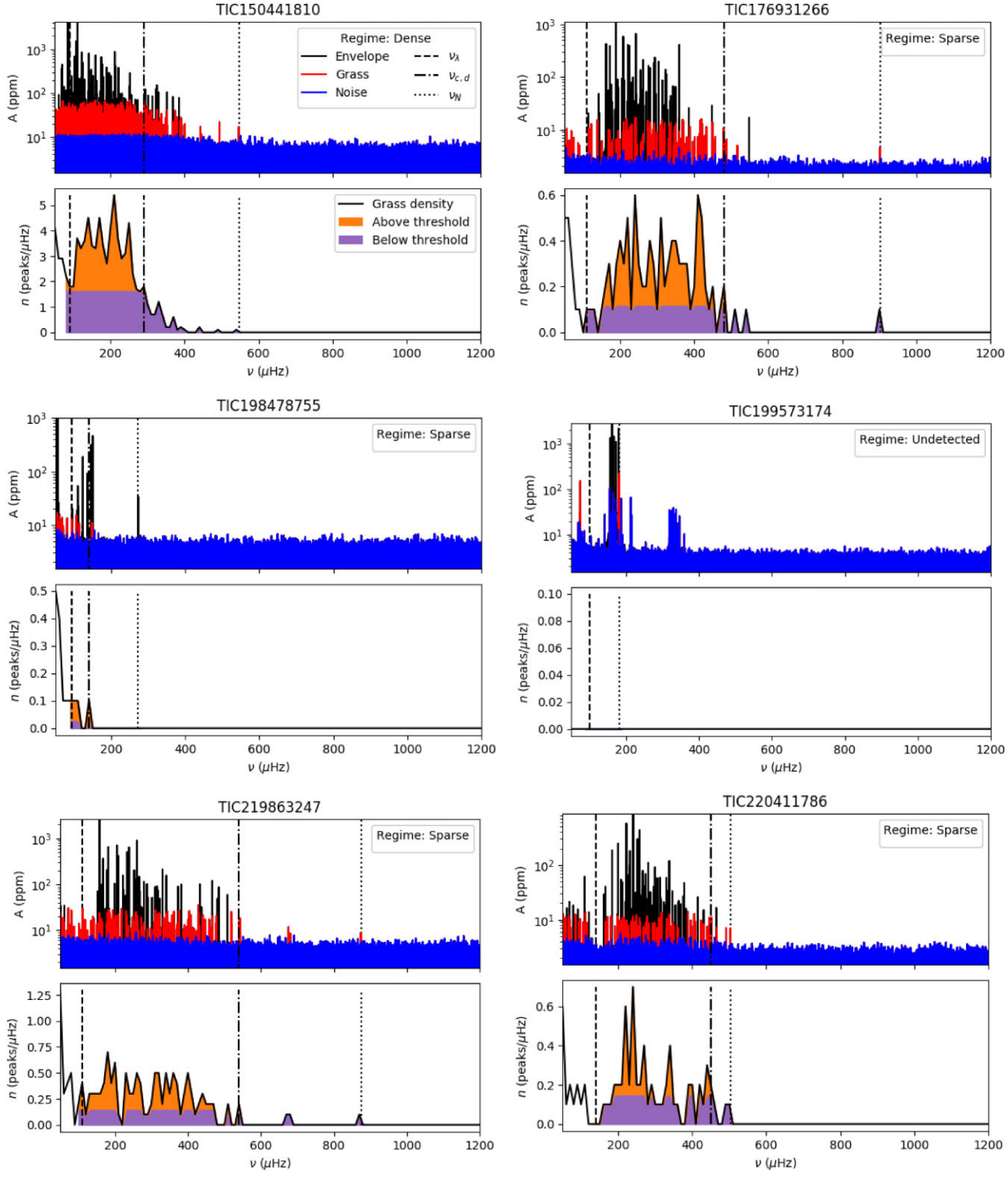

Figure B4 – *continued*

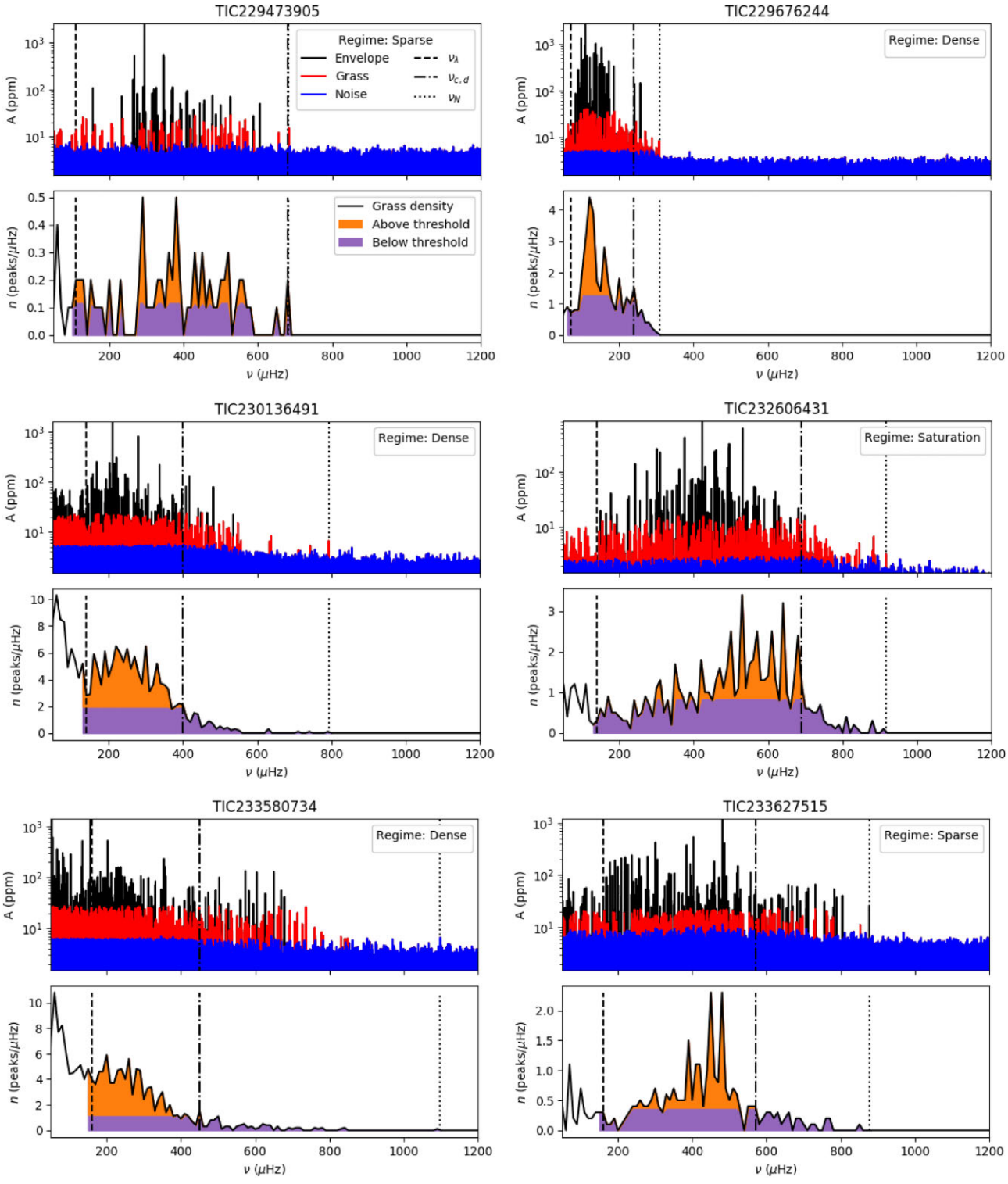

Figure B4 – *continued*

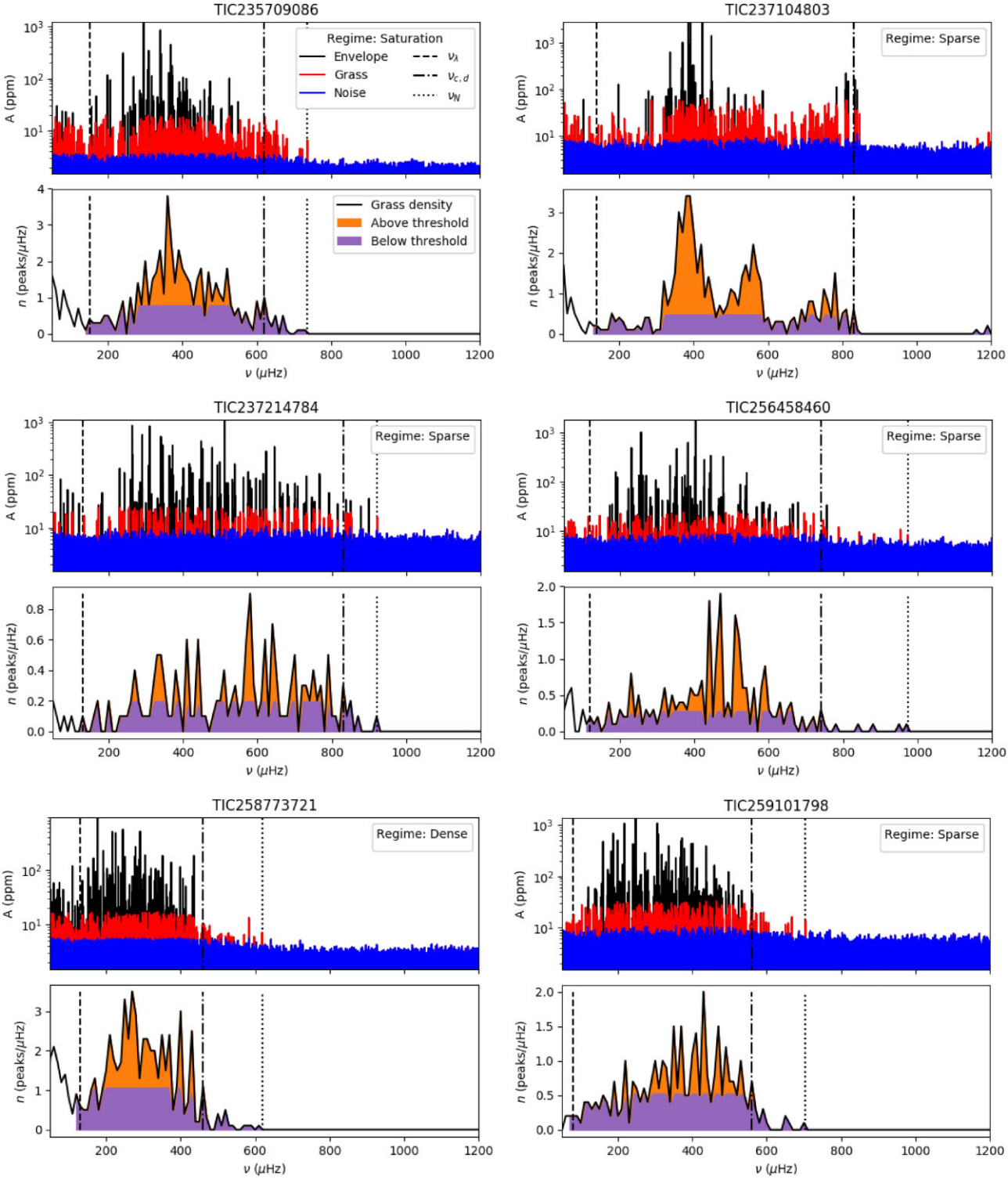

Figure B4 – *continued*

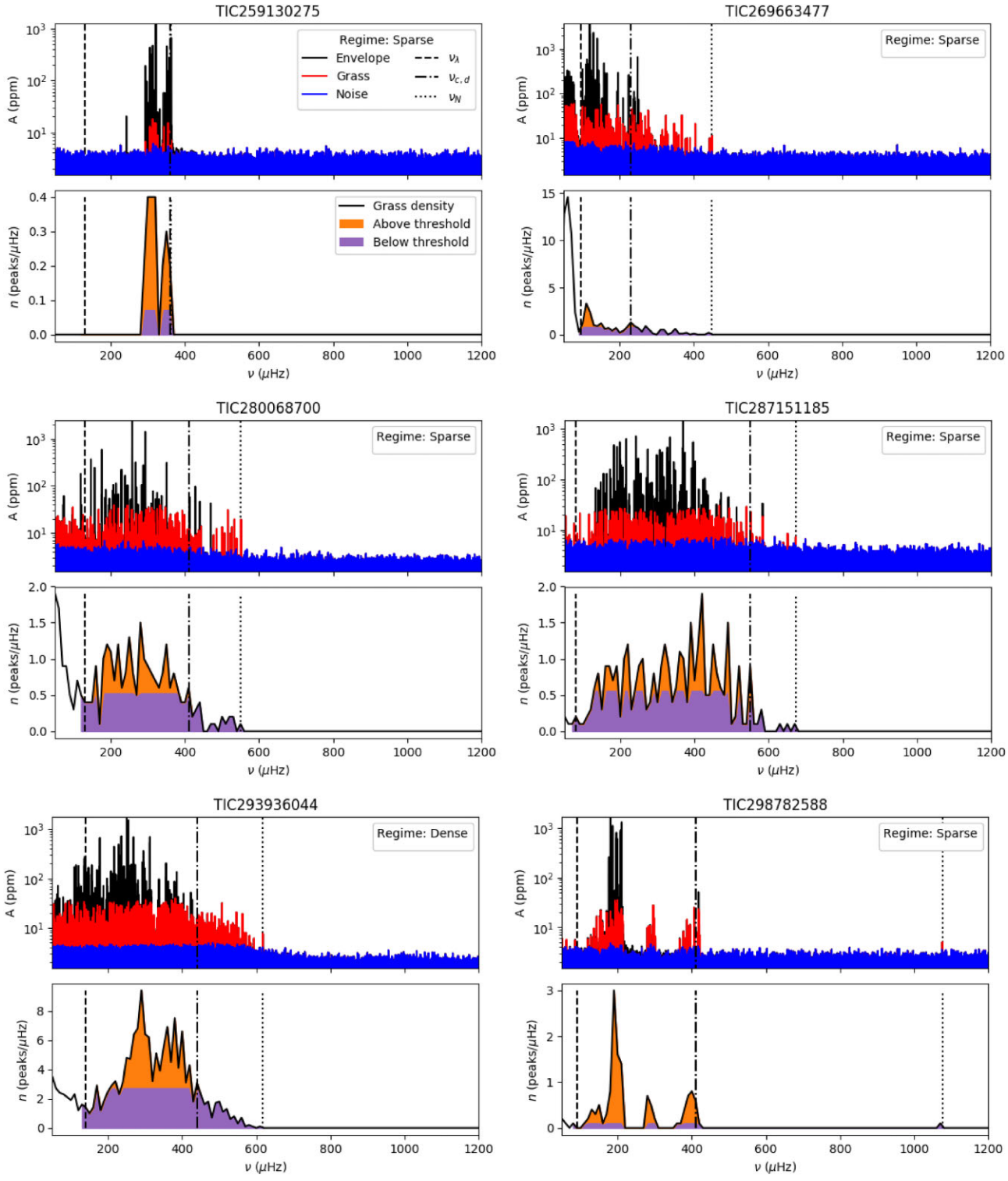

Figure B4 – *continued*

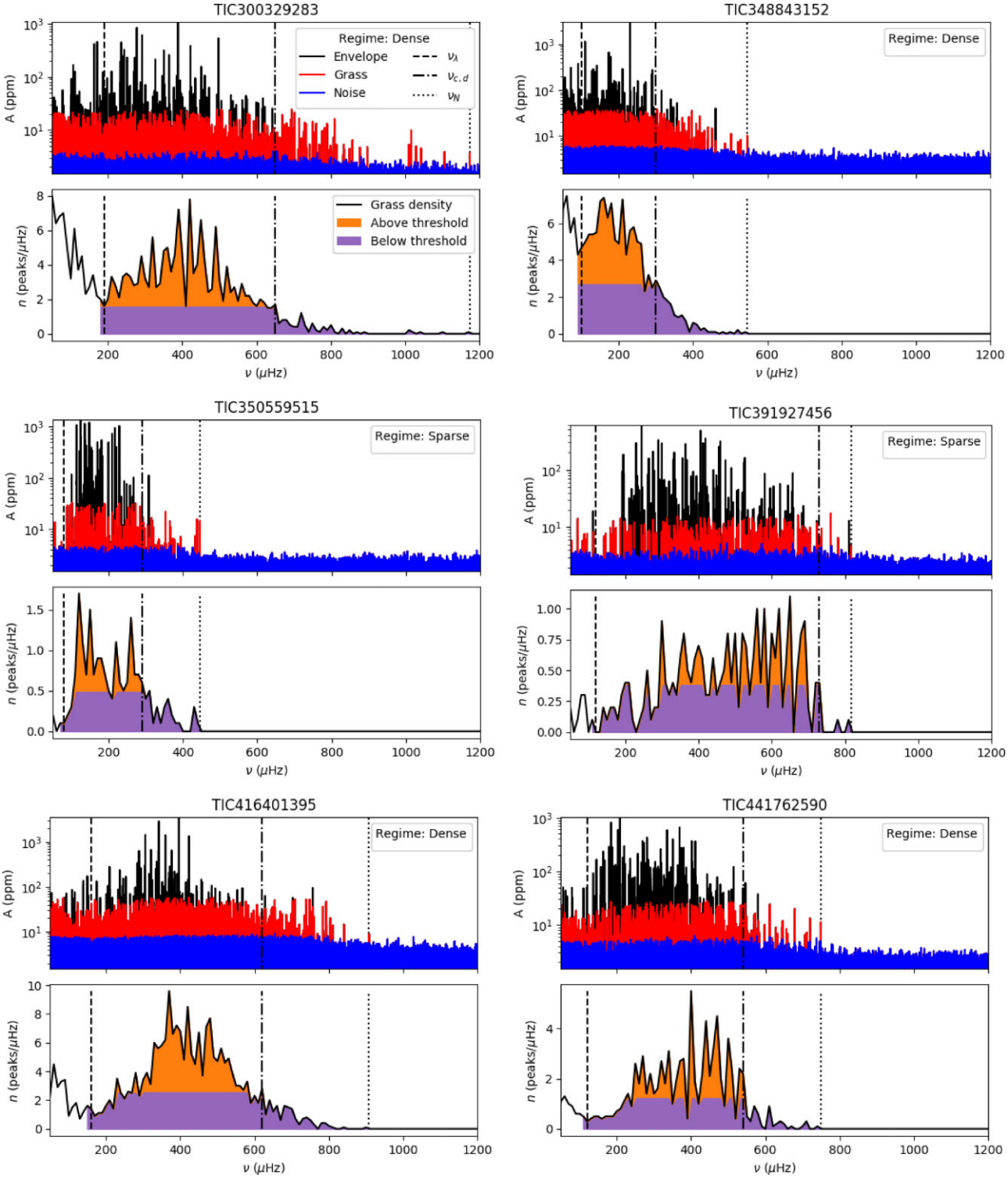

Figure B4 – *continued*

This paper has been typeset from a TEX/LATEX file prepared by the author.